

Exceptional band touching for strongly correlated systems in equilibrium

Tsuneaya Yoshida,¹ Robert Peters,² Norio Kawakami,² and Yasuhiro Hatsugai¹

¹*Department of Physics, University of Tsukuba, Ibaraki 305-8571, Japan*

²*Department of Physics, Kyoto University, Kyoto 606-8502, Japan*

(Dated: February 20, 2024)

Quasi-particles described by Green's functions of equilibrium systems exhibit non-Hermitian topological phenomena because of their finite lifetime. This non-Hermitian perspective on equilibrium systems provides new insights into correlated systems and attracts much interest because of its potential to solve open questions in correlated compounds. In this paper, we provide a concise review of the non-Hermitian topological band structures for quantum many-body systems in equilibrium as well as their classification.

CONTENTS

I. Introduction	2
II. Exceptional points for strongly correlated systems	3
A. Topological properties of EPs	3
1. Case of a 2×2 Hamiltonian	3
2. Topological invariant characterizing EPs	4
B. EPs appearing in the single-particle spectrum	5
C. EPs for two-dimensional heavy-fermion systems	5
III. Symmetry-protected exceptional rings and surfaces in correlated systems	7
A. Symmetry-protection of exceptional band touching	8
1. Case of a 2×2 Hamiltonian	8
2. Topological invariant characterizing SPERs and SPESs with chiral symmetry	9
B. SPERs for a correlated honeycomb lattice	10
C. SPESs for a correlated diamond lattice	12
IV. Ten-fold way classification of the exceptional band touching in equilibrium systems	14
A. Symmetry constraints	15
1. PT -symmetry	15
2. CP -symmetry	15
3. Chiral symmetry	16
B. Ten-fold way classification	16
1. Classification results	17
2. Details of the classification for the Hermitian Hamiltonian	17
V. Summary and outlook	19
VI. Acknowledgements	19
References	20

I. INTRODUCTION

After the discovery of topological insulators/superconductors, the topological perspective of condensed matter is of growing importance^{1–7}. While the notion of topology has been originally utilized to understand the band structure of a gapped quadratic Hamiltonian (i.e., free-fermion systems), it has been extended to gapless systems; it has elucidated that there exists topologically protected band touching for Weyl semi-metals^{8–11} or nodal line superconductors¹². The notion of topological phases has been further extended to correlated systems where correlations and topology induce a variety of exotic phenomena^{13–23}, such as topologically ordered systems^{24–36}, topological Mott insulators^{37–41}, and the reduction of topological classifications^{42–56}.

Intriguingly, recent studies have elucidated that correlations induce even non-Hermitian topological phenomena^{57–64} which are extensively analyzed in various contexts^{60,65–99} (e.g., photonic systems^{100–110}, open quantum systems^{111–124} etc.). In particular, Ref. 57 has pointed out that the finite lifetime of quasi-particles induces an exceptional point (EP) in the Brillouin zone (BZ) which is a representative example of the non-Hermitian topological band structure. Correspondingly, topologically protected band touching occurs both for the real and imaginary parts which we call exceptional band touching in this paper. The above EPs in many-body systems in equilibrium are connected by Fermi arcs, meaning that correlation induces the gapless excitations even for band insulators. The emergence of the EPs accompanied by the Fermi arcs is numerically demonstrated by applying the dynamical mean-field theory (DMFT) to heavy fermions⁵⁹. The above non-Hermitian perspective of Green's functions for equilibrium systems has been further developed with symmetry of many-body Hamiltonians^{60,91–94}; the interplay between symmetry and non-Hermiticity results in symmetry-protected exceptional rings (SPERs) in two dimensions⁶⁰ and symmetry-protected exceptional surfaces (SPESs) in three dimensions^{60,62}. The above recently developed non-Hermitian perspective in equilibrium systems attracts much interest because it provides new insights into quasi-particle spectrums which potentially solve open questions in condensed matter physics^{125–128}.

The aim of this article is to provide a concise review of these advances in the non-Hermitian perspective in correlated systems in equilibrium. As a 2×2 Hamiltonian describes the essential properties, we start with this simplest case and review numerical results demonstrating the emergence of exceptional band touching.

The rest of this paper is organized as follows. In Sec. II, we demonstrate the emergence of EPs for a heavy-fermion system by applying the DMFT to a heavy-fermion system. In Sec. III, we show that SPERs and SPESs can emerge for correlated systems with chiral symmetry. In Sec. IV, we address the ten-fold way classification of the exceptional band touching for single-particle spectrum by taking into account PT - (CP -) and chiral symmetry, where PT - (CP -) symmetry denotes the symmetry under the product of time-reversal and inversion (charge conjugation and inversion), respectively. A short summary and remaining open questions appear at the end of this paper.

II. EXCEPTIONAL POINTS FOR STRONGLY CORRELATED SYSTEMS

In this section, we elucidate that the EPs emerge due to finite lifetimes of quasi-particles for strongly correlated systems⁵⁹. Specifically, the origin of the above non-Hermitian topological phenomena is the imaginary part of the self-energy [see Eqs. (11) and (12)] which describes the lifetime of quasi-particles. The emergence of EPs results in the significant difference of the single-particle spectrum.

In the following, after a brief explanation of EPs (Sec. II A) and the single-particle Green's function (Sec. II B), we demonstrate the emergence of EPs for heavy-fermion systems and see that EPs significantly change the single-particle spectrum.

A. Topological properties of EPs

1. Case of a 2×2 Hamiltonian

Let us first analyze a non-Hermitian 2×2 Hamiltonian, which elucidates the essential properties of EPs.

It is well-known that a generic 2×2 matrix can be expanded by the Pauli matrices τ 's and the identity matrix τ_0

$$H(\mathbf{k}) = \sum_{\mu} [b_{\mu}(\mathbf{k}) + id_{\mu}(\mathbf{k})]\tau_{\mu}, \quad (1)$$

where b_{μ} and d_{μ} ($\mu = 0, 1, 2, 3$) are continuous functions taking real values.

One can numerically and analytically confirm that the above non-Hermitian matrix may show EPs. In Fig. 1, energy eigenvalues taking complex numbers are plotted for a specific choice of b 's and d 's. At the EPs, the Hamiltonian becomes non-diagonalizable. Correspondingly, as one can see in Fig. 1, the band touching occurs both for the real and imaginary parts of the energy eigenvalues.

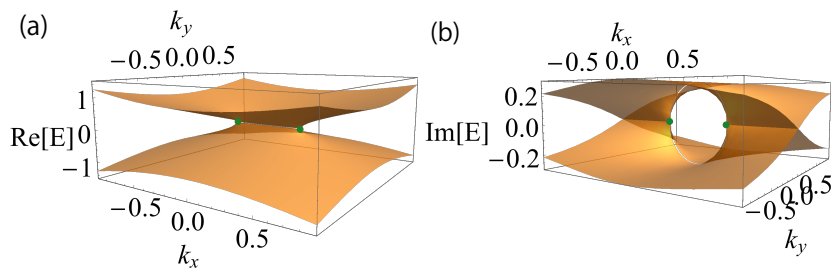


FIG. 1. Band structure of a continuum model for $(b_0, b_1, b_2, b_3) = (0, k_x, 0, k_y)$ and $(d_0, d_1, d_2, d_3) = (0, 0, 0, 0.3)$. In panel (a) [(b)] the real (imaginary) part of the energy is plotted, respectively. In these figures, the band touching points marked with green dots correspond to the EPs.

In order to see the details, we diagonalize the Hamiltonian (1), which yields

$$E_{\pm} = b_0 + id_0 \pm \sqrt{b^2 - d^2 + 2i\mathbf{b} \cdot \mathbf{d}}, \quad (2)$$

with $\mathbf{b} \cdot \mathbf{d} := \sum_{j=1,2,3} b_j d_j$, $b^2 = \mathbf{b} \cdot \mathbf{b}$ and $d^2 = \mathbf{d} \cdot \mathbf{d}$. The above equation indicates that band touching occurs both for the real and imaginary parts when the following conditions are satisfied

$$b^2 - d^2 = 0, \quad (3a)$$

$$\mathbf{b} \cdot \mathbf{d} = 0. \quad (3b)$$

In other words, the above conditions are necessary conditions for the emergence of EPs. One can see that the above conditions are indeed sufficient conditions; supposing that Eq. (3) is satisfied, we can see that the Hamiltonian can be rewritten as

$$H(\mathbf{k}) = (b_0 + id_0)\tau_0 + 2d \begin{pmatrix} 0 & 1 \\ 0 & 0 \end{pmatrix}, \quad (4)$$

with a proper choice of the basis. In this basis, one can see that the Hamiltonian is generically non-diagonalizable for $d \neq 0$.

In the above, we have seen the following facts. At the EP, the 2×2 Hamiltonian (1) becomes non-diagonalizable, resulting in the exceptional band touching. For the 2×2 Hamiltonian, the EP emerges if and only if Eqs. (3a) and (3b) are satisfied. We note that the band touching is protected by non-trivial topology whose topological invariant is discussed in the next subsection.

2. Topological invariant characterizing EPs

As shown in Fig. 1, the band touching occurs at the EPs. Such band touching for two-dimensional systems can be topologically characterized by the vorticity, akin to the winding number;

$$\nu = \frac{1}{4\pi i} \oint d^2\mathbf{k} \cdot \nabla_{\mathbf{k}} \log \det[H(\mathbf{k}) - E_0 \mathbb{1}]. \quad (5)$$

Here, we have considered that the band touching occurs at energy E_0 . $H(\mathbf{k})$ ($\dim H \geq 2$) denotes a generic non-Hermitian matrix. $\nabla_{\mathbf{k}} := (\partial_{k_x}, \partial_{k_y})$. The path of the integral is chosen so that it encloses the EP. For $\dim H = 2$, the vorticity can be written as^{74,129}

$$\nu = \frac{1}{2\pi} \oint d^2\mathbf{k} \cdot \nabla_{\mathbf{k}} \arg[E_+(\mathbf{k}) - E_-(\mathbf{k})], \quad (6)$$

where E_{\pm} is the energy eigenvalue [see Eq. (2)].

In the following, we see how the vorticity defined in Eq. (5) characterizes the EPs. Consider a generic non-Hermitian matrix $H(\mathbf{k})$ with $\dim H \geq 2$ which shows the band touching at energy E_0 . The band touching point can be formulated as

$$\det[H(\mathbf{k}_0) - E_0 \mathbb{1}] = 0, \quad (7)$$

where \mathbf{k}_0 denotes the EP in the momentum space. Mapping the non-Hermitian Hamiltonian to the Hermitian matrix \tilde{H} , we can rewrite the above condition as

$$\det[\tilde{H}(\mathbf{k}_0)] = 0, \quad (8a)$$

with

$$\tilde{H} = \begin{pmatrix} 0 & H(\mathbf{k}) - E_0 \mathbb{1} \\ H^\dagger(\mathbf{k}) - E_0^* \mathbb{1} & 0 \end{pmatrix}_\rho. \quad (8b)$$

Here, we have extended the Hilbert space on which the Pauli matrices ρ 's act. This can be easily confirmed by noticing that Eq. (8a) can be written as $|\det[H(\mathbf{k}_0) - E_0]|^2 = 0$. The above fact means that the exceptional band touching can be described by the zero modes of the Hermitian matrix \tilde{H} which is chiral symmetric $\{\tilde{H}, \tilde{\Sigma}\} = 0$ with $\tilde{\Sigma} := \mathbb{1} \otimes \rho_3$. Therefore, remembering that the zero modes of the chiral symmetric Hermitian Hamiltonian are characterized by the winding number,

$$\nu_W = \frac{1}{4\pi i} \oint d^2\mathbf{k} \cdot \text{tr}[\tilde{\Sigma} \tilde{H}^{-1} \nabla_{\mathbf{k}} \tilde{H}], \quad (9)$$

we can see that the EPs can be characterized by the vorticity (5); substituting $\tilde{\Sigma} = \mathbb{1} \otimes \rho_3$ to Eq. (9) yields Eq. (5)¹³⁰. We note that the vorticity is half-quantized due to the extra prefactor $1/2$, which is just a convention.

In this section, we have considered two-dimensional systems. We note, however, that the vorticity is well-defined along a one-dimensional path in the three-dimensional BZ. In this case, the vorticity characterizes exceptional loops in the BZ (see also Table I). For a 2×2 Hamiltonian, there is complimentary understanding. The EPs appear when both of Eqs. (3a) and (3b) are satisfied, meaning that one degree of freedom is left in the three dimensions. This remaining degree of freedom forms a loop which is nothing but the exceptional loop in three dimensions.

B. EPs appearing in the single-particle spectrum

In the above, we have seen that a non-Hermitian matrix may show EPs which are characterized by the vorticity (5). In this section, we see that a non-Hermitian matrix governs the single-particle excitation spectrum of correlated systems in equilibrium (i.e., the energy is conserved).

Firstly, we define the retarded single-particle Green's function $G^R(t, \mathbf{k})$ whose imaginary part corresponds to the single-particle spectrum:

$$G_{\alpha\beta}^R(t, \mathbf{k}) = -i\langle \hat{c}_{\mathbf{k}\alpha}(t)\hat{c}_{\mathbf{k}\beta}^\dagger(0) + \hat{c}_{\mathbf{k}\beta}^\dagger(0)\hat{c}_{\mathbf{k}\alpha}(t) \rangle \theta(t), \quad (10)$$

where $\hat{c}_{\mathbf{k}\alpha}^\dagger$ creates a fermion with momentum \mathbf{k} in the state α (spin, orbital etc.). $\langle \cdot \rangle$ denotes the expectation value for temperature β^{-1} [$\langle \cdot \rangle := \text{tr}(\cdot e^{-\beta\hat{H}})$]. $\hat{c}_{\mathbf{k}\alpha}^\dagger(t) := e^{i\hat{H}t}\hat{c}_{\mathbf{k}\alpha}^\dagger e^{-i\hat{H}t}$ with the second quantized Hamiltonian \hat{H} describing the correlated system in equilibrium (i.e., \hat{H} is a Hermitian operator). $\theta(t)$ takes 0, 1/2, and 1 for $t < 0$, $t = 0$, and $t > 0$, respectively. Applying the Fourier transformation, we obtain the Dyson's equation¹³¹:

$$G^{-1}(\omega + i\delta, \mathbf{k}) = g^{-1}(\omega + i\delta, \mathbf{k}) - \Sigma(\omega + i\delta, \mathbf{k}), \quad (11)$$

which defines the self-energy $\Sigma(\omega + i\delta, \mathbf{k})$. Here, $g(\omega + i\delta, \mathbf{k})$ denotes the retarded Green's function for free fermions. δ is an infinitesimal constant ($\delta > 0$). With the Green's function, the single-particle spectral function is defined as $A(\omega, \mathbf{k}) = -\text{Im} \sum_{\alpha} G_{\alpha\alpha}(\omega + i\delta, \mathbf{k})/\pi$, which can be rewritten as

$$A(\omega, \mathbf{k}) = -\frac{1}{\pi} \text{Im} \text{tr}[(\omega + i\delta)\mathbb{1} - H_{\text{eff}}(\omega, \mathbf{k})]^{-1}, \quad (12a)$$

$$H_{\text{eff}}(\omega, \mathbf{k}) = h(\mathbf{k}) + \Sigma(\omega + i\delta, \mathbf{k}). \quad (12b)$$

Here, the matrix $h(\mathbf{k})$ is the Bloch Hamiltonian for free fermions with momentum \mathbf{k} . $\mathbb{1}$ denotes the identity matrix. We note that the self-energy $\Sigma(\omega + i\delta, \mathbf{k})$ is a non-Hermitian matrix, describing the lifetimes of quasi-particles. Therefore, Eq. (12a) indicates that the single-particle excitations of energy ω are governed by the non-Hermitian matrix $H_{\text{eff}}(\omega, \mathbf{k})$.

In addition to EPs, the non-Hermiticity of the effective Hamiltonian yields low energy excitations. The energy gap can be pure imaginary because of the non-Hermiticity of H_{eff} . In this case, even when the Bloch Hamiltonian is gapped, the system may show Fermi arcs connecting EPs.

We finish this section by making a comment on an additional condition for the EPs in the single-particle spectrum. The effective Hamiltonian appears in the denominator of the spectral weight (12a), meaning that the EPs are seriously smeared when the denominator is large. Therefore, in order for EPs to emerge as a peak in the single-particle spectral function, the frequency ω should satisfy an additional condition [for instance see Eq. (17a)].

C. EPs for two-dimensional heavy-fermion systems

In this section, we demonstrate that EPs emerge in the single-particle spectrum of a heavy-fermion system, by employing the DMFT. In particular, we analyze the Kondo lattice in two dimensions. The Hamiltonian reads,

$$\hat{H} = \sum_{\langle ij \rangle \alpha, \beta} t_{i\alpha, j\beta} \hat{c}_{i\alpha s}^\dagger \hat{c}_{j\beta s} + J \sum_i \hat{\mathbf{s}}_{ib} \cdot \hat{\mathbf{S}}_i, \quad (13)$$

where $\hat{c}_{i\alpha s}^\dagger$ creates an electron with spin $s = \uparrow, \downarrow$ in orbital $\alpha = a, b$ of site i . $\hat{\mathbf{s}}_{ib} := \frac{1}{2} \hat{c}_{ib s}^\dagger \boldsymbol{\sigma}_{ss'} \hat{c}_{ib s'}$ with the Pauli matrices $\boldsymbol{\sigma}$'s acting on the spin space. $\hat{\mathbf{S}}$ is the spin 1/2 operator for the localized spins. Here, the Kondo coupling of electrons in orbital a is neglected for simplicity. The hopping $t_{i\alpha, j\beta}$ is defined so that the Bloch Hamiltonian is written as

$$h(\mathbf{k}) = -2t' \sin k_y \tau_1 + [-\epsilon_0 - 2t(\cos k_x + \cos k_y)]\tau_3, \quad (14)$$

where ϵ_0 , t , and t' take real values, respectively. The Pauli matrices τ 's act on the orbital space. In the non-interacting case, this model shows two Dirac cones for $t = 1$ and $0 < \epsilon_0 < 4$.

In order to analyze the above correlated electron system, we employ the DMFT^{132–135} which treats local correlation exactly. In the DMFT framework, the lattice model is mapped to an effective impurity model where the self-energy of spin s [$\Sigma_s(\omega + i\delta) := \text{diag}(0, \Sigma_{bs}(\omega + i\delta))$] is computed self-consistently¹³⁶. Here, $\Sigma_{bs}(\omega + i\delta)$ denotes the self-energy for orbital b and spin s . In order to compute the self-energy for the effective impurity model, we employ the

numerical renormalization group method (NRG)^{137–139}. This method directly provides the single-particle spectral function, while other methods based on Monte Carlo calculations^{140–142} require the analytic continuation.

Once the self-energy is obtained, the single-particle spectrum is obtained as

$$A(\omega, \mathbf{k}) = -\frac{1}{\pi} \text{Im tr}[(\omega + i\delta)\mathbb{1} - H_{\text{eff}}(\omega, \mathbf{k})]^{-1}, \quad (15a)$$

$$H_{\text{eff}}(\omega, \mathbf{k}) = h(\mathbf{k}) + \Sigma(\omega + i\delta). \quad (15b)$$

Here, we have omitted the subscript s [$\Sigma(\omega + i\delta) := \text{diag}(0, \Sigma_b(\omega + i\delta))$] by assuming that the system is in the paramagnetic phase. We note that the effective Hamiltonian is a 2×2 matrix. Expanding it with the Pauli matrices as Eq. (1), we obtain the following coefficients

$$(b_0, b_1, b_2, b_3) = \left(\frac{\text{Re}\Sigma_b(\omega + i\delta)}{2}, 2t' \sin k_y, 0, -\epsilon_0 - 2t(\cos k_x + \cos k_y) - \frac{\text{Re}\Sigma_b(\omega + i\delta)}{2} \right), \quad (16a)$$

$$(d_0, d_1, d_2, d_3) = \left(\frac{\text{Im}\Sigma_b(\omega + i\delta)}{2}, 0, 0, -\frac{\text{Im}\Sigma_b(\omega + i\delta)}{2} \right). \quad (16b)$$

Therefore, the conditions for EPs appearing as the peak of the single-particle spectral function are written as

$$2\omega_0 - \text{Re}\Sigma_b(\omega_0 + i\delta) = 0, \quad (17a)$$

$$-\epsilon_0 - 2t(\cos k_{0x} + \cos k_{0y}) - \frac{\text{Re}\Sigma_b(\omega_0 + i\delta)}{2} = 0, \quad (17b)$$

$$-[\text{Im}\Sigma_b(\omega_0 + i\delta)]^2 + 16t'^2 \sin^2 k_{0y} = 0. \quad (17c)$$

Here, the second and the third equations are obtained from Eq. (3), specifying the position of the EP \mathbf{k}_0 in the BZ. The first equation specifies the energy ω_0 where the EPs emerge as peaks of the spectral function. We note that in the DMFT framework, the momentum dependence of the self-energy is neglected. However, the EPs should emerge even in calculations beyond the DMFT framework because they are topologically protected.

Let us now analyze the Kondo lattice model (13). In the rest of this section, we set the parameters to $(t, t', \epsilon_0) = (1, 0.667, 0.667)$. The obtained phase diagram is shown in Fig. 2. When the Kondo coupling is small, an anti-ferromagnetic phase emerges because the Ruderman-Kittel-Kasuya-Yosida interaction^{143–145} becomes dominant. Increasing the interaction J , itinerant electrons and localized spins form singlets due to the Kondo effect. As a result, the anti-ferromagnetic phase is suppressed in the region of strong J .

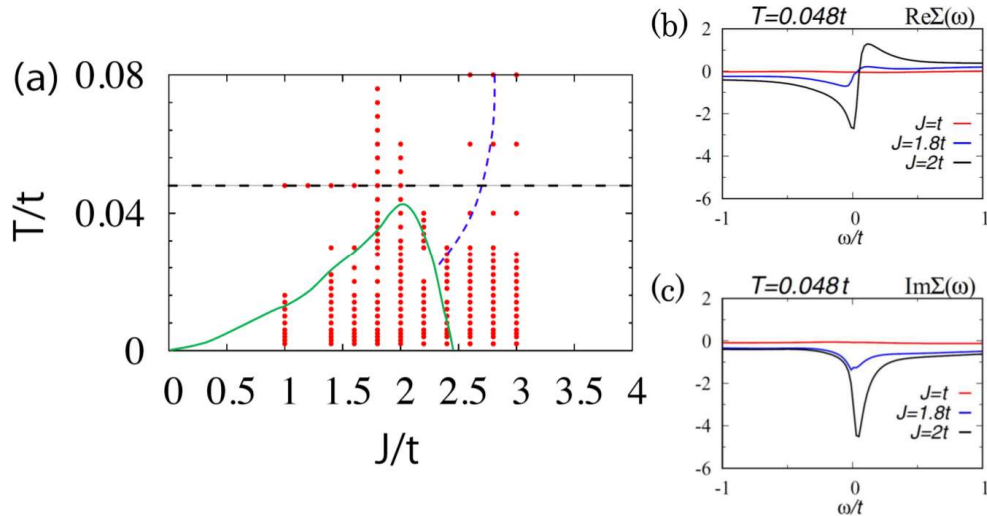


FIG. 2. (a) Phase diagram of the Kondo coupling J vs. the temperature T . The Neel temperature is represented with the solid green line. The Kondo temperature is represented with the dashed blue line. The horizontal dashed line denotes the region of $T = 0.048t$. (b) [(c)] The real (imaginary) part of the self-energy for several values of the coupling J at $T = 0.048t$, respectively. These figures are adapted with permission from Ref. 59. Copyright 2018 American Physical Society.

We numerically observe the EPs in the paramagnetic phase. The Kondo effect plays an important role for the emergence of EPs. The self-energy is shown in Figs. 2(b) and 2(c) for $T = 0.048t$ which corresponds to the horizontal line in Fig. 2(a). For small J ($J = t$), the real and imaginary parts of the self-energy take small values because the

electrons are almost decoupled from the localized spins. Increasing the coupling J enhances the Kondo effect, which results in a dip structure of $\text{Im}\Sigma_b(\omega + i\delta)$ in the low-energy region (i.e., around $\omega \sim 0$). This dip structure of the self-energy induces the EPs. The single-particle spectral function for $J = 1.8t$ is plotted in Fig. 3. Firstly, we show the data obtained by assuming that the imaginary part of the self-energy is zero [see Fig. 3(a)] in order to show that the imaginary part of the self-energy is essential for the EPs. In this figure, we can see a single peak due to the existence of a Dirac cone. Fig. 3(b) shows the spectral function obtained by the DMFT. In this figure, we can see that the dip structure of the imaginary part splits the Dirac cone into two EPs as represented with green dots. Furthermore, we can see that the EPs are connected by the Fermi arc where the bulk gap $\Delta_c = E_+ - E_-$ becomes pure imaginary. The emergence of the Fermi arc enhances the local density of states around $\omega \sim 0$ [see Fig. 4(a)]. In the above, we have seen that the imaginary part of the self-energy splits each of two Dirac cones into a pair of EPs connected with the bulk Fermi arc. As we see below, these bulk Fermi arcs are robust because the EPs are topologically protected.

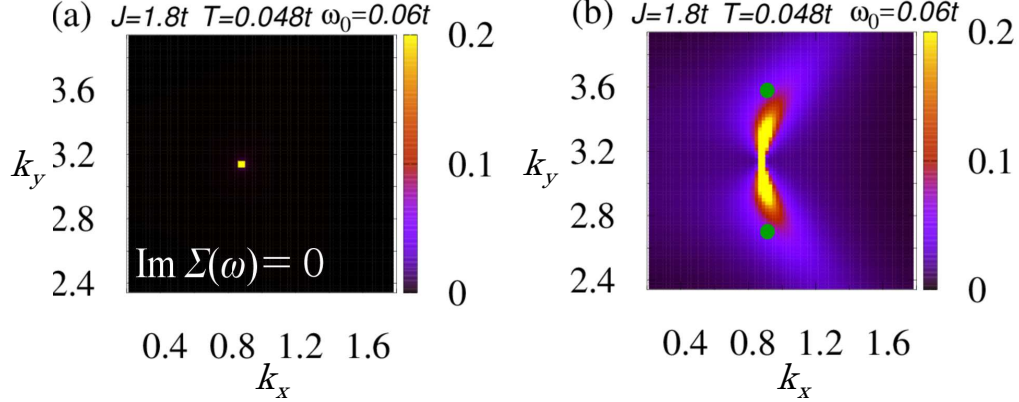


FIG. 3. Single-particle spectral function $A(\omega_0, \mathbf{k})$ with $\omega_0 = 0.06t$ for $J = 1.8t$ and $T = 0.048t$. The data are plotted around the boundary of the BZ ($k_y = \pi$). Panel (a) is plotted by setting the imaginary part of the self-energy to zero $\text{Im}\Sigma_b(\omega_0) = 0$. In this figure, we can see that the peak for $k_y = \pi$, indicating the emergence of the Dirac cone with chiral symmetry. Panel (b) shows that the Dirac cone splits into two EPs (green dots) because of the imaginary part of the self-energy. These EPs are connected with Fermi arcs. These figures are adapted with permission from Ref. 59. Copyright 2018 American Physical Society.

Here, we address the characterization of the above EPs. Because the vorticity is written as Eq. (6) for the 2×2 Hamiltonian, we can compute its value by plotting the argument of Δ_c^2 [see Fig. 4(b)]. In this figure, the branch cut of Δ_c is represented with white dashed lines which end at EPs. Therefore, taking the integral along the green line illustrated in Fig. 4(b), we can see that the vorticity takes $\nu = -1/2$. We note that the vorticity takes $\nu = 1/2$ for the EP around $k_x = -\pi/2$.

Changing the Kondo coupling results in pair annihilation of EPs. Here, we note that there are two scenarios: (i) a pair of EPs originating from a Dirac point are annihilated by themselves; (ii) two pairs EPs exchange the pairs and are annihilated. The former scenario can be observed by decreasing the Kondo coupling J . In Fig. 5(a), we can see that two EPs approach and are annihilated. Correspondingly, the Fermi arc vanishes. The latter scenario can be observed by increasing the interaction J . When the Kondo effect is enhanced, the EPs approach the boundary of the BZ specified by $k_x = \pi$. On this boundary, the pair of EPs arising from two distinct Dirac cones annihilate each other [see Fig. 5(b)]. The qualitative difference from the previous case is that a Fermi loop emerges after the pair annihilation of EPs, enhancing the LDOS in the low-energy region [see Fig. 6(a)]. The emergence of the Fermi loop is again due to the energy gap taking a value of pure imaginary [see Fig. 6(b)].

III. SYMMETRY-PROTECTED EXCEPTIONAL RINGS AND SURFACES IN CORRELATED SYSTEMS

In the previous section, we have seen that electron correlations induce EPs in the absence of symmetry. In addition, it is well-known that the symmetry enriches the topological structures for Hermitian systems^{146–149}. Therefore, it should be valuable to analyze the effects of symmetry on EPs, which is the main subject of this section.

Ref. 60 has revealed that many-body chiral symmetry results in novel types of exceptional band touching, SPERs in two dimensions and SPESs in three dimensions. In the following, after elucidating the topological properties of SPERs and SPESs, we demonstrate the emergence of them in correlated systems.

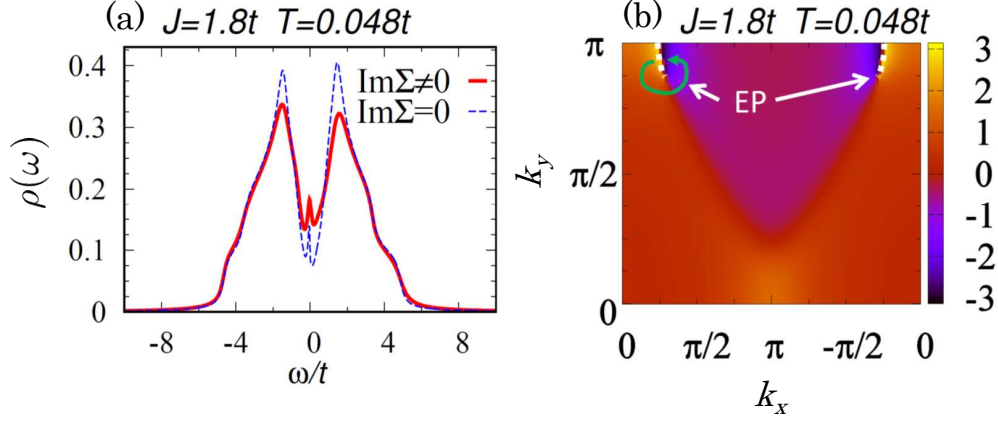


FIG. 4. (a) The local density of states $\rho(\omega) = \sum_{\mathbf{k}} A(\omega, \mathbf{k})/N$ for $J = 2$ and $T = 0.048t$. Here, N denotes the number of unit cells. The red line indicates the data computed with the obtained self-energy. For comparison, we also plot the data obtained by setting $\text{Im}\Sigma_b(\omega) = 0$ (see blue line). (b) Color map of $\text{Arg}[\Delta_c^2(\omega_0, \mathbf{k})]$ with $\omega_0 = 0.06t$. On white dashed lines, the value $\text{Arg}[\Delta_c^2(k_x, k_y)]$ jumps from $-\pi$ to π which corresponds to the branch cut of Δ_c . These figures are adapted with permission from Ref. 59. Copyright 2018 American Physical Society.

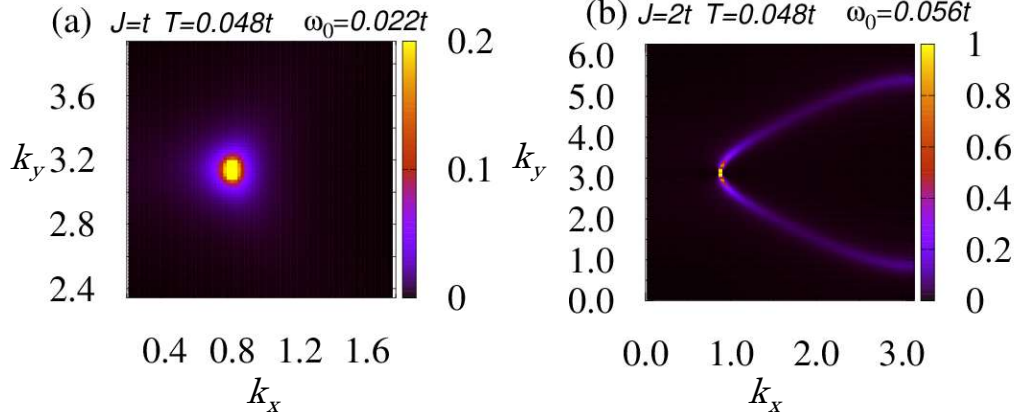


FIG. 5. The single-particle spectral function $A(\omega_0, \mathbf{k})$ for $T = 0.048t$. Data for $J = t$ and $J = 2t$ are plotted in panel (a) and (b), respectively. Panel (a) indicates that the Fermi arc shrinks, corresponding to the fusion of two EPs. Panel (b) indicates that the Fermi loop emerges because two EPs merge at the boundary of the BZ. These figures are adapted with permission from Ref. 59. Copyright 2018 American Physical Society.

A. Symmetry-protection of exceptional band touching

1. Case of a 2×2 Hamiltonian

Firstly, we analyze a case of the 2×2 Hamiltonian [see Eq. (1)] which captures the essential properties. Here, let us suppose that the Hamiltonian for a two-dimensional system satisfies the following relation

$$\tau_3 H^\dagger(\mathbf{k}) \tau_3 = -H(\mathbf{k}), \quad (18)$$

which indicates that the system is chiral symmetric [see Eq. (29a)]. The above condition imposes the following symmetry condition on the coefficients, b 's and d 's:

$$b_0 = b_3 = d_1 = d_2 = 0. \quad (19)$$

Now, let us consider effects of the symmetry constraint on the EPs. As we have seen in Sec. II A 1, EPs emerge when the two conditions Eqs. (3a) and (3b) are satisfied. We note, however, that one of the conditions, Eq. (3b), is always satisfied by the symmetry constraint, meaning that the number of the conditions for the EPs is reduced. This

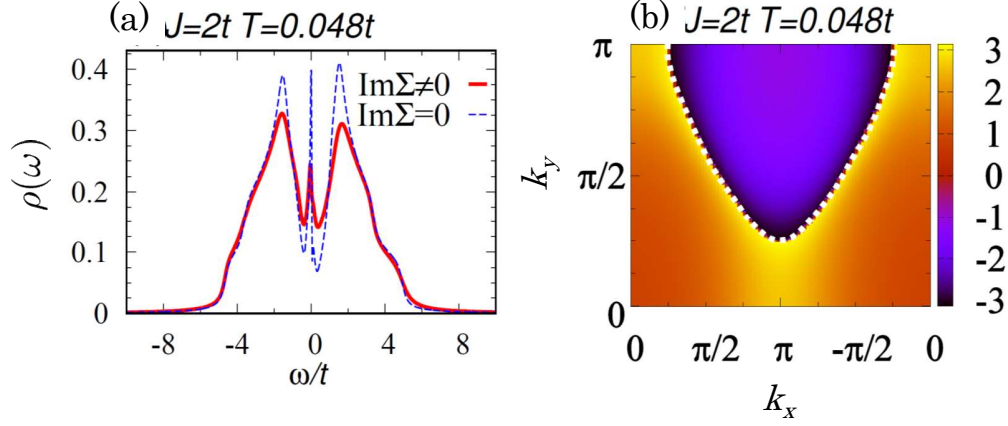


FIG. 6. (a) The local density of states $\rho(\omega) = \sum_{\mathbf{k}} A(\omega, \mathbf{k})/N$ for $J = 2t$ and $T = 0.048t$. Here, N denotes the number of unit cells. The red line indicates the data computed with the obtained self-energy. For comparison, we plot the data obtained by setting $\text{Im}\Sigma_b(\omega) = 0$ (see blue line). (b) Color map of $\text{Arg}[\Delta_c^2(k_x, k_y)]$. On the white dashed lines, the value $\text{Arg}[\Delta_c^2(k_x, k_y)]$ jumps from $-\pi$ to π . For this parameter set, the white dashed line forms a closed loop. These figures are adapted with permission from Ref. 59. Copyright 2018 American Physical Society.

fact indicates that for the two-dimensional BZ, fixing one degree of freedom is sufficient to obtain the EPs. Therefore, the remaining degree of freedom forms a ring of EPs which is denoted as a SPER⁶⁰. On an arbitrary point of the SPERs, the band touching occurs both for the real and imaginary parts.

We can apply the same argument to a three-dimensional system where SPESs emerge⁶⁰. In this case, the two degrees of freedom are left in the BZ.

2. Topological invariant characterizing SPERs and SPESs with chiral symmetry

In the above, we have seen that the symmetry constraint results in SPERs or SPESs where the exceptional band touching occurs. In this section, we show that the band touching is topologically characterized by the zero-th Chern number, a zero-dimensional topological invariant.

Let us suppose that the $2n \times 2n$ Hamiltonian satisfies the following relation

$$U_{\Gamma} H^{\dagger}(\mathbf{k}) U_{\Gamma}^{\dagger} = -H(\mathbf{k}), \quad (20)$$

where U_{Γ} is a unitary matrix satisfying $U_{\Gamma}^2 = \mathbb{1}$. The above equation is a generic form of the symmetry constraint (18). We now consider the following Hermitian Hamiltonian composed of $H(\mathbf{k})$;

$$\tilde{H}(\mathbf{k}) = \begin{pmatrix} 0 & H(\mathbf{k}) - E_0 \\ H^{\dagger}(\mathbf{k}) - E_0^* & 0 \end{pmatrix}_{\rho}, \quad (21)$$

where we have assumed that the exceptional band touching occurs at energy $E_0 \in i\mathbb{R}$. In a similar way to the case of Sec. II A 2, we can define the topological invariant characterizing the SPERs and SPESs by addressing topological characterization of zero energy excitations described by the Hermitian Hamiltonian \tilde{H} . The essential difference from the previous case (Sec. II A 2) is that the Hermitian Hamiltonian preserves the two distinct constraints of chiral symmetry;

$$\tilde{\Sigma} \tilde{H}(\mathbf{k}) \tilde{\Sigma}^{-1} = -\tilde{H}(\mathbf{k}), \quad (22a)$$

$$\tilde{U}_{\Gamma} \tilde{H}(\mathbf{k}) \tilde{U}_{\Gamma}^{-1} = -\tilde{H}(\mathbf{k}), \quad (22b)$$

with

$$\tilde{\Sigma} = \mathbb{1} \otimes \rho_3, \quad (22c)$$

$$\tilde{U}_{\Gamma} = U_{\Gamma} \otimes \rho_1. \quad (22d)$$

The additional chiral symmetry allows us to define the zero-th Chern number. Due to two distinct constraints of chiral symmetry, the Hamiltonian can be block-diagonalized with a unitary operator $\tilde{U} = i\tilde{\Sigma}\tilde{U}_\Gamma$ ($\tilde{U}^2 = \mathbb{1}$),

$$\tilde{H} = \begin{pmatrix} H_+ & 0 \\ 0 & H_- \end{pmatrix}. \quad (23)$$

Here, H_+ (H_-) denotes the Hamiltonian acting on the subspace where the operator \tilde{U} is reduced to $\mathbb{1}$ ($-\mathbb{1}$), respectively. We denote these subspaces by plus and minus sectors. We note that applying either $\tilde{\Sigma}$ or \tilde{U}_Γ exchanges the plus and minus sectors because of the anti-commutation relation $\{\tilde{U}_\Gamma, \tilde{\Sigma}\} = \{\tilde{\Sigma}, \tilde{U}\} = 0$. Namely, letting $|+\rangle$ be a state of the plus sector ($\tilde{U}|+\rangle = |+\rangle$), we obtain $\tilde{U}\tilde{\Sigma}|+\rangle = -\tilde{\Sigma}|+\rangle$, which means that $\tilde{\Sigma}|+\rangle$ belongs to the minus sector. The above facts indicate that the block-diagonalized Hamiltonians H_+ and H_- are related to each other and belong to symmetry class A. Therefore, the characterization of the zero energy excitations of $\tilde{H}(\mathbf{k})$ can be done with the zero-th Chern number for the plus sector which corresponds to the number of the eigenstates with negative eigenvalues of H_+ . This fact suggests \mathbb{Z} classification of zero-dimensional Hermitian systems belonging to class A.

We note that the block-diagonalized Hamiltonian is rewritten as $H_+ = iU_\Gamma H$, which can be seen as follows. Noticing that the unitary matrix V block-diagonalizes the unitary operator $\tilde{U} = U_\Gamma \otimes \rho_2$,

$$\tilde{V}^\dagger \tilde{U} \tilde{V} = \begin{pmatrix} \mathbb{1} & 0 \\ 0 & -\mathbb{1} \end{pmatrix}, \quad (24a)$$

with

$$\tilde{V} = \frac{1}{\sqrt{2}} \begin{pmatrix} \mathbb{1} & -i\mathbb{1} \\ iU_\Gamma & -U_\Gamma \end{pmatrix}_\rho, \quad (24b)$$

we can block-diagonalize the Hermitian Hamiltonian \tilde{H} :

$$\tilde{V}^\dagger \tilde{H} \tilde{V} = \begin{pmatrix} iHU_\Gamma & 0 \\ 0 & -HU_\Gamma \end{pmatrix}. \quad (25)$$

Here, we have used the relation $U_\Gamma^2 = \mathbb{1}$.

Therefore, the SPERs and the SPEs are characterized by the zero-th Chern number which is the number of negative eigenvalues of the Hermitian Hamiltonian $H_+(\mathbf{k}) = iH(\mathbf{k})U_\Gamma$ at each point in the BZ.

The above result indicates that the dimension of the objects composed of the exceptional band touching becomes one-dimensional higher by chiral symmetry [Eq. (20)] compared to system without the symmetry (see Table I). Table I

dimension	1	2	3
no symmetry	-	point	loop
with chiral symmetry	point	ring	surface

TABLE I. Objects formed by EPs in the BZ for each case of spatial dimensions. In the presence of chiral symmetry, exceptional band touching forms objects which are one-dimensional higher than the ones in the absence of symmetry.

also indicates that the EPs emerging in one-dimensional systems are either unstable or symmetry-protected.

We finish this section with the complementary understanding for the 2×2 Hamiltonian. Namely, exceptional band touching appears at points where both of Eqs. (3a) and (3b) are satisfied. Thus, in the absence of symmetry, exceptional band touching forms $(d-2)$ -dimensional objects in the d -dimensional BZ. On the other hand, in the presence of chiral symmetry, exceptional band touching forms $(d-1)$ -dimensional objects because Eq. (3b) is always satisfied by symmetry.

B. SPERs for a correlated honeycomb lattice

The SPERs can emerge for strongly correlated systems in equilibrium. In order to demonstrate the emergence of the SPERs, we apply the DMFT+NRG to a Hubbard model of a honeycomb lattice. The Hamiltonian reads

$$\hat{H} = \sum_{\langle ij \rangle \alpha \beta} t_{i\alpha, j\beta} \hat{c}_{i\alpha s}^\dagger \hat{c}_{j\beta s'} + \sum_{i\alpha} U_\alpha \left(\hat{n}_{i\alpha\uparrow} - \frac{1}{2} \right) \left(\hat{n}_{i\alpha\downarrow} - \frac{1}{2} \right), \quad (26)$$

where $\hat{c}_{i\alpha s}^\dagger$ creates a fermion with spin $s = \uparrow, \downarrow$ at site i and sublattice $\alpha = A, B$. $\hat{n}_{i\alpha\uparrow} := \hat{c}_{i\alpha s}^\dagger \hat{c}_{i\alpha s}$. The first term describes the nearest-neighbor hopping with $t_{i\alpha, j\beta} \in \mathbb{R}$. The second term describes the on-site repulsion ($U_\alpha \geq 0$). Applying the Fourier transformation for $U_\alpha = 0$, we obtain the Bloch Hamiltonian which is written as

$$h(\mathbf{k}) = b_1(\mathbf{k})\tau_1 + b_2(\mathbf{k})\tau_2, \quad (27a)$$

where $b_1(\mathbf{k})$ and $b_2(\mathbf{k})$ [$b_1(\mathbf{k}), b_2(\mathbf{k}) \in \mathbb{R}$] are defined as

$$b_1(\mathbf{k}) - ib_2(\mathbf{k}) = te^{i\mathbf{k} \cdot \mathbf{a}_1} + t'e^{i\mathbf{k} \cdot \mathbf{a}_2} + t'e^{i\mathbf{k} \cdot \mathbf{a}_3}. \quad (27b)$$

Here, we have assumed the hopping t ($t' := rt$) between sites connected with gray (brown) lines, respectively. Vectors \mathbf{a} 's are illustrated in Fig. 7. We consider that this model can be fabricated for cold atoms because the inhomogeneous Hubbard interaction is implemented with the optical Feshbach resonance^{150,151}.

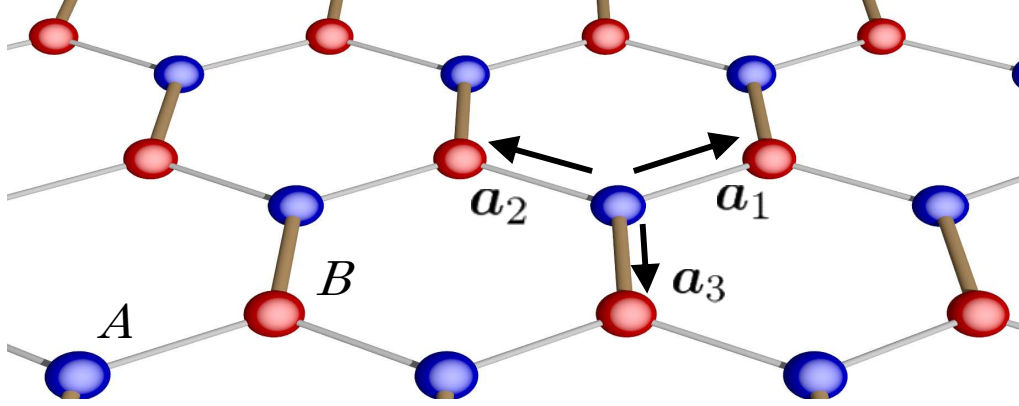


FIG. 7. Sketch of the honeycomb Hubbard model. The A - (B -) sublattice is illustrated with blue (red) spheres, respectively. Vectors \mathbf{a}_1 , \mathbf{a}_2 , and \mathbf{a}_3 specify the neighboring sites; $\mathbf{a}_1 := (\sqrt{3}, 1)/2$, $\mathbf{a}_2 := (-\sqrt{3}, 1)/2$, and $\mathbf{a}_3 := (0, -1)$. Nearest-neighbor hopping with t (rt) is represented with gray (brown) bonds, respectively. This figure is adapted with permission from Ref. 60. Copyright 2019 American Physical Society.

The above model preserves the chiral symmetry for an arbitrary value of the interaction U_α :

$$\hat{\Gamma} \hat{H} \hat{\Gamma}^{-1} = \hat{H}, \quad (28a)$$

$$\hat{\Gamma} = \prod_{j\alpha} \left(\hat{c}_{j\alpha\uparrow}^\dagger + \text{sgn}(\alpha) \hat{c}_{j\alpha\uparrow} \right) \left(\hat{c}_{j\alpha\downarrow}^\dagger + \text{sgn}(\alpha) \hat{c}_{j\alpha\downarrow} \right), \quad (28b)$$

with $\text{sgn}(\alpha)$ taking 1 (−1) for $\alpha = A$ ($\alpha = B$), respectively. This symmetry imposes the following constraint on the Green's function

$$\tau_3 G(-\omega + i\delta, \mathbf{k}) \tau_3 = -G(\omega + i\delta, \mathbf{k}). \quad (29a)$$

In particular, for $\omega = 0$, the above condition can be rewritten as

$$\tau_3 H_{\text{eff}}^\dagger(0, \mathbf{k}) \tau_3 = -H_{\text{eff}}(0, \mathbf{k}), \quad (29b)$$

in terms of the effective Hamiltonian $H_{\text{eff}}(\omega, \mathbf{k})$. This constraint is nothing but the symmetry discussed in the previous section [see Eq. (18)]. Therefore, the chiral symmetry of the correlated systems (28) protects the SPERs emerging in the single-particle spectrum.

The DMFT results elucidate the emergence of the SPERs. In Fig. 8, the spectrum at $\omega = 0$ is plotted for several values of the temperature. In the non-interacting case, it is well-known that the Dirac cones appear at the corners of the BZ illustrated with the white hexagon. In the presence of the correlations, the Dirac cones split into rings [see green rings in Fig. 8(a)]. Increasing the temperature suppresses the lifetimes of quasi-particles. Correspondingly, the SPERs become large [Fig. 8(b)]. In this figure, we can also see the effect of symmetry on the Fermi arcs shown in Fig. 3(b). Because of the chiral symmetry, the Fermi arcs change into the Fermi planes. This is because the energy eigenvalues E_n appear in a pair ($E_n, -E_n^*$) or become pure imaginary in the presence of the chiral symmetry (29b)¹⁵².

For higher temperatures, the SPERs, arising from distinct Dirac cones, merge into the single loop [see Fig. 3(c)]. We also note that the presence of the Dirac cones is not a necessary condition for the SPERs. Introducing the anisotropy

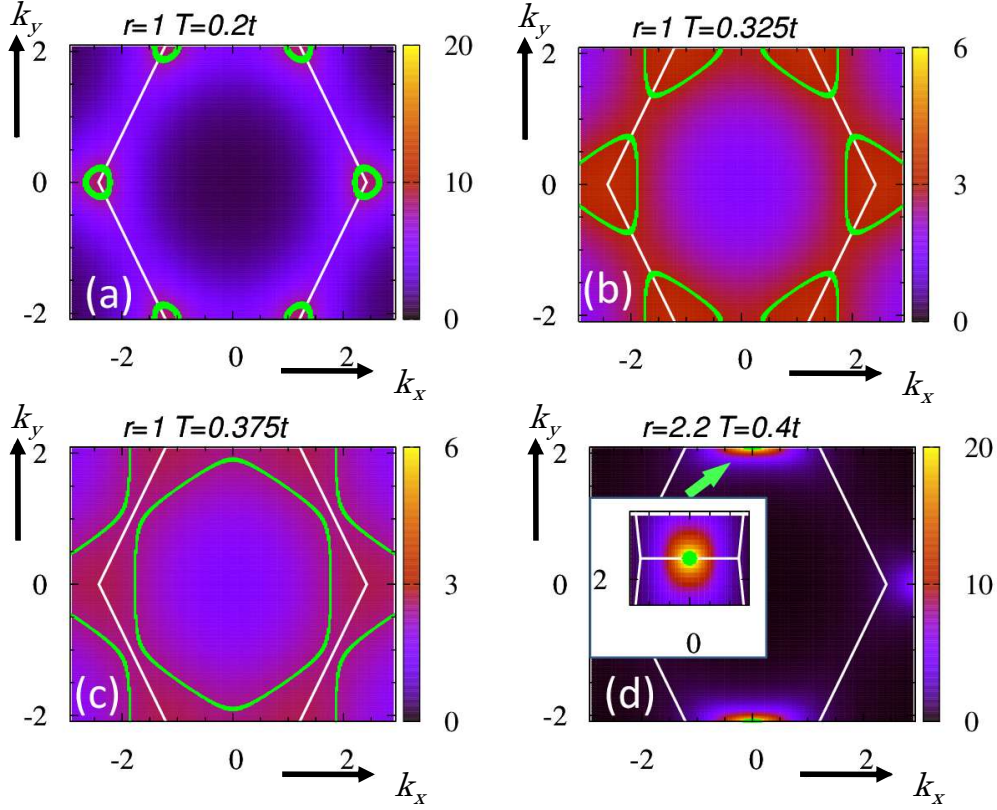


FIG. 8. The single-particle spectral function $[A(\omega = 0, \mathbf{k})]$ for several values of temperature. Panels (a)-(c) show data for $r = 1$ while panel (d) shows data for $r = 2.2$ where the system does not host Dirac cones. These data are obtained for $U_A = 10t$ and $U_B = 5t$. In these figures, the SPERs are shown with green lines. In the region enclosed with the rings, the energy gap becomes pure imaginary. The BZ is illustrated with the white hexagon. These figures are adapted with permission from Ref. 60. Copyright 2019 American Physical Society.

of the hopping, the Dirac cones disappear because of the pair annihilation. Even in the absence of the Dirac cones the SPERs emerge [see Fig. 8(d)]. We note that the SPERs are topologically stable; Fig. 9(a) shows that the numerical characterization of the SPERs with the zero-th Chern number can be done.

Finally we show that the emergence of Fermi plane accompanying the SPER enhances the specific heat $C = d\langle H \rangle / dT$ because the Fermi plane induces additional low energy excitations. In Fig. 9(b), the specific heat is shown with the red line. For comparison, we also plot data with the blue line by assuming that the imaginary part of self-energy for A - and B -sublattices takes the average value $\text{Im}[\Sigma_A(\omega + i\delta) + \Sigma_B(\omega + i\delta)]/2$. We note that the system does not show SPERs when the imaginary part for A -sublattice is identical to that for B -sublattice. In this figure, we can see that the specific heat is enhanced because of the Fermi planes accompanying SPERs.

C. SPESs for a correlated diamond lattice

The emergence of the SPESs can also be demonstrated by applying the DMFT to a Hubbard model of a diamond lattice, which is a three-dimensional extension of the honeycomb Hubbard model (26). The lattice structure and the BZ is shown in Fig. 10(a) and 10(b), respectively. In a similar way as the previous section, we introduce an inhomogeneity of the interaction.

In the following, we see the details. For $U_A = 8t$, $U_B = 0$, and $T = 0.8t$, the SPESs emerge as shown in Fig. 10(c). Here, we have employed the iterative perturbation method^{153,154} as the impurity solver of the DMFT. In the following, we see the results in detail. In Fig. 11(a), the single-particle spectral function at zero energy $A(\omega = 0, \mathbf{k})$ is plotted for the k_{xy} - k_z plane [i.e., the blue plane in Fig. 10(b)]. The green dots plotted in Fig. 11(a) correspond to the sections of SPESs. We note that in the region enclosed with the SPESs, the energy gap becomes pure imaginary, meaning that the zero energy excitations appear in this region. Thus, the Fermi volume appears instead of the Fermi arc discussed in Sec. II C. Fig. 11(b) shows the single-particle spectral function $A(\omega, \mathbf{k})$ along the lines connecting the

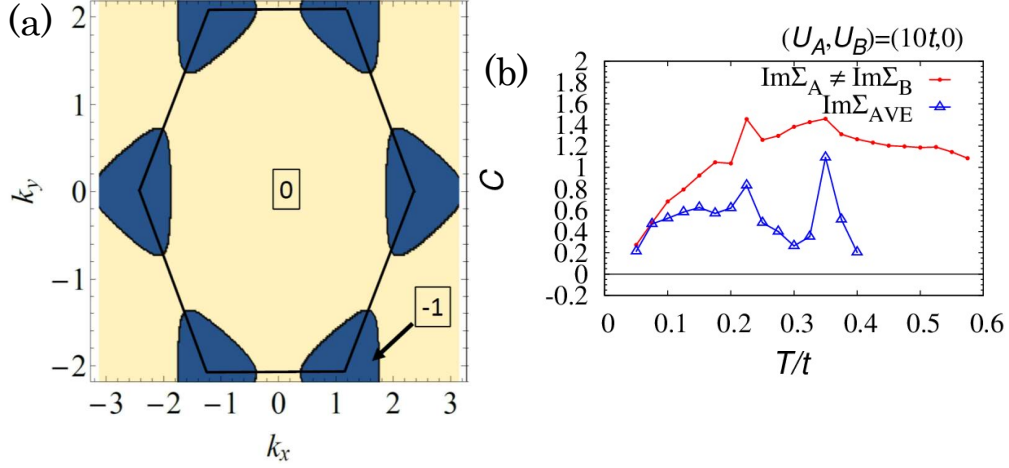


FIG. 9. (a) Colormap of the zero-th Chern number for $r = 1$, $T = 0.0325t$, $U_A = 10t$, and $U_B = 5t$. Black lines represent the SPERs separating domains where the zero-th Chern number takes distinct values. The black hexagon illustrates the BZ. The numbers enclosed with black squares denote the zero-th Chern number which is defined so that it takes zero for the Hermitian case $H_{\text{eff}} = b_1\tau_1 + b_2\tau_2$. (b) Temperature dependence of the specific heat for $r = 1$, $U_A = 10t$, and $U_B = 0$. Data plotted with the blue line is for comparison; the data are obtained by assuming that the imaginary part of the self-energy takes the same value $\text{Im}[\Sigma_A(\omega) + \Sigma_B(\omega)]/2$. Namely, the data of blue line do not show the SPERs. Fermi planes emerge for $T \gtrsim 0.1$. These figures are adapted with permission from Ref. 60. Copyright 2019 American Physical Society.

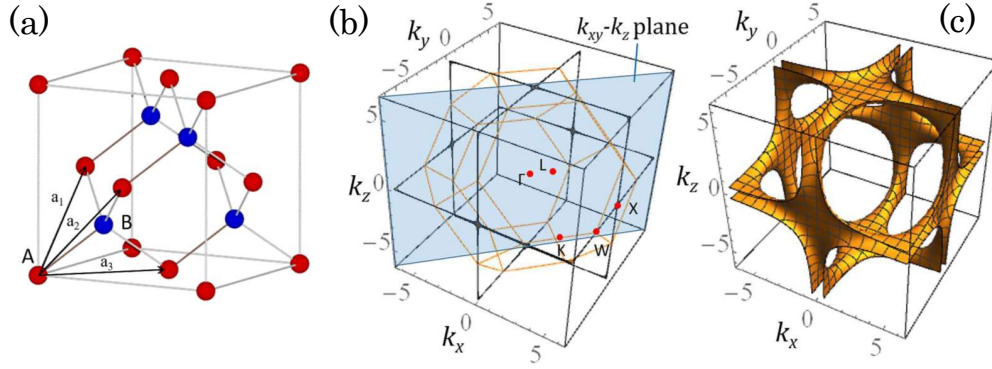


FIG. 10. (Color Online). (a) Sketch of the diamond lattice. This lattice is composed of two sublattices, A and B which are illustrated with red and blue spheres, respectively. We assume that interaction for A -sublattice is stronger than that of B -sublattice. (b) The BZ and the high symmetric points for the diamond lattice. The BZ is illustrated with orange lines. (c) Exceptional surface for $U_A = 8t$, $U_B = 0$, and $T = 0.8t$. These figures are adapted with permission from Ref. 62. Copyright 2019 American Physical Society.

high symmetry points in the BZ. In this figure, we can confirm the emergence of the Fermi volume by the presence of the zero energy excitations between X and K points. Outside of the SPESs, the zero energy excitations disappear.

We finish this section with a comment concerning the effect of SPESs on the magnetic response. As shown in Fig. 11(c), the LDOS of the B -sublattice is enhanced by the Fermi volume accompanying the SPESs. We note that the LDOS of the A -sublattice is just renormalized. This imbalance of the LDOS can induce a counterintuitive behavior of the local magnetic susceptibility. In Fig. 11(b), the local magnetic susceptibility computed with the random-phase approximation (RPA)¹⁵⁵ is plotted. As shown in Fig. 11(d), due to the imbalance of the LDOS, the magnetic susceptibility of the B -sublattice becomes larger than that of the A -sublattice, although the interaction of the B -sublattice is weaker than that of the A -sublattice.

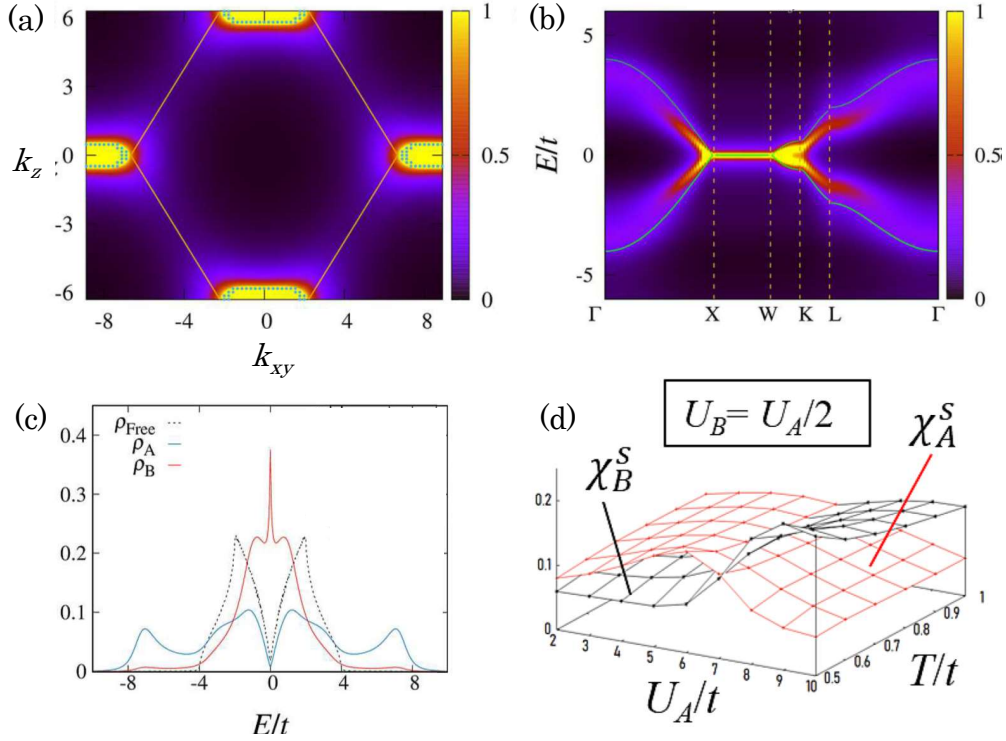


FIG. 11. (Color Online). Spectral properties and the magnetic response. (a) The single-particle spectral function $A(\omega=0, \mathbf{k})$ for the k_{xy} - k_z plane shown in Fig. 10(b). (b) The single-particle spectral function $A(\omega, \mathbf{k})$ along the lines connecting high symmetry points in the BZ. The blue lines in this panel illustrate the dispersion relation for the non-interacting case. (c) The local density of states $\rho_\alpha(\omega) = -\sum_{\mathbf{k}} \text{Im} G_{\alpha\alpha}(\omega, \mathbf{k}) / (\pi N)$ with N denoting the number of unit cells. Data shown in panels (a), (b), and (c) are obtained for $U_A = 8t$, $U_B = 0$, and $T = 0.8t$. (d) Magnetic susceptibility χ_α^s against interaction U_A and temperature T . Here, U_B is set to $U_B = U_A/2$. For the detailed calculation of the susceptibility, see footnote 155. These figures are adapted with permission from Ref. 62. Copyright 2019 American Physical Society.

IV. TEN-FOLD WAY CLASSIFICATION OF THE EXCEPTIONAL BAND TOUCHING IN EQUILIBRIUM SYSTEMS

In Sec. III, we have seen that the correlated systems with chiral symmetry may show SPERs and SPESs in two and three dimensions, respectively. These SPERs and SPESs are characterized by the zero-th Chern number, a zero-dimensional topological invariant taking an arbitrary integer (see Sec. III A 2). In other words, the topological classification of the exceptional band touching is \mathbb{Z} for the system with chiral symmetry.

In this section, by generalizing the argument in Sec. III, we address the topological classification of the exceptional band touching. Specifically, we carry out the ten-fold way classification^{146–149} of exceptional band touching in the presence/absence of PT -, CP -, and chiral symmetry for correlated systems. This is because PT - (CP -) symmetry is closed at each point in the BZ as well as the chiral symmetry (i.e., the corresponding symmetry transformation does no flip the momentum). We note that the 38-fold way classification for exceptional band touching is carried out in Ref. 94 for a generic Bloch Hamiltonian. However, our analysis clarifies which symmetry classes are relevant for correlated systems. Our ten-fold way classification is consistent with the corresponding classification results for 38 symmetry classes.

In what follows, we address the classification of exceptional band touching after a brief description of the relevant symmetry.

A. Symmetry constraints

1. PT -symmetry

For the correlated systems preserving PT -symmetry (i.e., symmetry under the product of time-reversal and spatial inversion), the second quantized Hamiltonian \hat{H} satisfies

$$\widehat{PT}\hat{H}\widehat{PT}^{-1} = \hat{H}. \quad (30)$$

Here, the anti-unitary operator \widehat{PT} is written as

$$\widehat{PT} = \hat{U}_{PT}\mathcal{K}, \quad (31a)$$

$$\hat{U}_{PT}\hat{c}_{i\alpha}^\dagger\hat{U}_{PT}^\dagger = \sum_{\beta}\hat{c}_{-i\beta}^\dagger U_{PT,\beta\alpha}, \quad (31b)$$

where $\hat{c}_{i\alpha}^\dagger$ creates a fermion with state α at site i . \hat{U}_{PT} is a unitary operator. \mathcal{K} is an operator taking complex conjugation. U_{PT} is a matrix satisfying $U_{PT}U_{PT}^* = \pm\mathbb{1}$. Here we have supposed that under the inversion, site j is mapped to $-j$.

For PT -symmetric systems, the Green's function satisfies²⁰

$$G(\omega + i\delta, \mathbf{k}) = U_{PT}G^T(\omega + i\delta, \mathbf{k})U_{PT}^\dagger, \quad (32a)$$

which can be rewritten as

$$H_{\text{eff}}(\omega + i\delta, \mathbf{k}) = U_{PT}H_{\text{eff}}^T(\omega + i\delta, \mathbf{k})U_{PT}^\dagger. \quad (32b)$$

Eq. (32a) can be seen by a straightforward calculation¹⁵⁶.

2. CP -symmetry

For correlated systems preserving CP -symmetry (i.e., symmetry under the product of charge conjugation and inversion), the second quantized Hamiltonian \hat{H} satisfies

$$\widehat{CP}\hat{H}\widehat{CP}^{-1} = \hat{H}, \quad (33)$$

with \widehat{CP} corresponding to the unitary operator $\widehat{CP} = \hat{U}_{CP}$ which transforms $\hat{c}_{i\alpha}$ as

$$\hat{U}_{CP}\hat{c}_{i\alpha}\hat{U}_{CP}^\dagger = \sum_{\beta}\hat{c}_{-i\beta}^\dagger U_{CP,\beta\alpha}.$$

Here, U_{CP} is a unitary matrix satisfying $U_{CP}U_{CP}^* = \pm\mathbb{1}$.

For CP -symmetric systems, the Green's function satisfies

$$G(\omega + i\delta, \mathbf{k}) = -U_{CP}G^*(-\omega + i\delta, \mathbf{k})U_{CP}^\dagger, \quad (34a)$$

which can be rewritten as

$$H_{\text{eff}}(\omega + i\delta, \mathbf{k}) = -U_{CP}H_{\text{eff}}^*(-\omega + i\delta, \mathbf{k})U_{CP}^\dagger. \quad (34b)$$

Eq. (34a) can be obtained by using the following relations:

$$G(\omega + i\delta) = -U_{CP}G^T(-\omega - i\delta)U_{CP}^\dagger, \quad (35)$$

and

$$G_{\alpha\beta}^*(\omega - i\delta, \mathbf{k}) = G_{\beta\alpha}(\omega + i\delta, \mathbf{k}). \quad (36)$$

We note that applying the Fourier transformation, $G(-\omega - i\delta, \mathbf{k})$ is rewritten as $G^A(-t, \mathbf{k})$ which is defined as

$$G_{\alpha\beta}^A(t, \mathbf{k}) := i\langle\hat{c}_{\mathbf{k}\alpha}(t)\hat{c}_{\mathbf{k}\beta}^\dagger + \hat{c}_{\mathbf{k}\beta}^\dagger\hat{c}_{\mathbf{k}\alpha}(t)\rangle\theta(-t). \quad (37)$$

Eqs. (35) and (36) are obtained by straightforward calculations^{157,158}.

3. Chiral symmetry

For the correlated systems preserving chiral symmetry, the second quantized Hamiltonian \hat{H} satisfies

$$\hat{\Gamma}\hat{H}\hat{\Gamma}^{-1} = \hat{H}, \quad (38a)$$

with

$$\hat{\Gamma} = \hat{U}_\Gamma \mathcal{K}. \quad (38b)$$

Here, \hat{U}_Γ is a unitary operator transforming the annihilation operator as

$$\hat{U}_\Gamma \hat{c}_{i\alpha} \hat{U}_\Gamma^\dagger = \sum_\beta \hat{c}_{i\beta}^\dagger U_{\Gamma, \beta\alpha}, \quad (38c)$$

where U_Γ is a matrix satisfying $U_\Gamma^2 = \mathbb{1}$.

For chiral symmetric systems, the Green's function satisfies

$$G(\omega + i\delta, \mathbf{k}) = -U_\Gamma G^\dagger(-\omega + i\delta, \mathbf{k}) U_\Gamma^\dagger, \quad (39a)$$

which can be rewritten as

$$H_{\text{eff}}(\omega + i\delta, \mathbf{k}) = -U_\Gamma H_{\text{eff}}^\dagger(-\omega + i\delta, \mathbf{k}) U_\Gamma^\dagger. \quad (39b)$$

Eq. (32a) can be obtained by a straightforward calculation¹⁵⁹. This equation can also be obtained from Eqs. (32a) and (34a) by noticing that applying the operator $\hat{\Gamma}$ is equivalent to applying the product of the operators \widehat{PT} and \widehat{CP} .

B. Ten-fold way classification

Prior to the topological classification of exceptional band touching, we note the following two facts. (i) Exceptional band touching of the non-Hermitian Hamiltonian $H_{\text{eff}}(\omega = 0, \mathbf{k})$ can be described by a Hermitian Hamiltonian satisfying $\{\tilde{H}, \tilde{\Sigma}\} = 0$ with $\tilde{\Sigma} = \mathbb{1} \otimes \rho_3$ [see e.g., Eq. (8b)]^{87,89,90,94,160,161}. (ii) For Hermitian systems, the classification of d_{EP} -dimensional gapless excitations in d spatial dimensions is accomplished by classifying the $\delta - 1$ dimensional gapped Hermitian Hamiltonian with $\delta = d - d_{\text{EP}}$ ^{162,163}.

Thus, the problem is reduced to classifying gapless excitations of the Hermitian Hamiltonian \tilde{H} in the presence/absence of the following symmetry constraints:

$$\tilde{U}_{PT} \tilde{H}^*(\mathbf{k}) \tilde{U}_{PT}^\dagger = \tilde{H}(\mathbf{k}), \quad (40a)$$

$$\tilde{U}_{CP} \tilde{H}^*(\mathbf{k}) \tilde{U}_{CP}^\dagger = -\tilde{H}(\mathbf{k}), \quad (40b)$$

$$\tilde{U}_\Gamma \tilde{H}^*(\mathbf{k}) \tilde{U}_\Gamma^\dagger = -\tilde{H}(\mathbf{k}), \quad (40c)$$

with

$$\tilde{H} = \begin{pmatrix} 0 & H_{\text{eff}}(0, \mathbf{k}) \\ H_{\text{eff}}^\dagger(0, \mathbf{k}) & 0 \end{pmatrix}_\rho, \quad (40d)$$

$$\tilde{U}_{PT} = \begin{pmatrix} 0 & U_{PT} \\ U_{PT}^\dagger & 0 \end{pmatrix}_\rho, \quad (40e)$$

$$\tilde{U}_{CP} = U_{CP} \rho_0, \quad (40f)$$

$$\tilde{U}_\Gamma = \begin{pmatrix} 0 & U_\Gamma \\ U_\Gamma^\dagger & 0 \end{pmatrix}_\rho, \quad (40g)$$

and $\tilde{U}_{PT} \tilde{U}_{PT}^* = \pm \mathbb{1}$, $\tilde{U}_{CP} \tilde{U}_{CP}^* = \pm \mathbb{1}$, and $\tilde{U}_\Gamma \tilde{U}_\Gamma = \mathbb{1}$.

The above relation can also be written with the two anti-unitary operators ($\widetilde{PT} = \tilde{U}_{PT} \mathcal{K}$, and $\widetilde{CP} = \tilde{U}_{CP} \mathcal{K}$) and a unitary operator ($\tilde{\Gamma} := \tilde{U}_\Gamma$). We note that the above unitary matrices (\tilde{U}_{PT} , \tilde{U}_{CP} , and \tilde{U}_Γ) satisfy the following commutation/anti-commutation relations:

$$\{\tilde{U}_{PT}, \tilde{\Sigma}\} = 0, \quad (41a)$$

$$[\tilde{U}_{CP}, \tilde{\Sigma}] = 0, \quad (41b)$$

$$\{\tilde{U}_\Gamma, \tilde{\Sigma}\} = 0. \quad (41c)$$

Therefore, exceptional band touching can be classified by addressing the classification of gapless excitations in Hermitian systems with additional chiral symmetry whose operator $\tilde{\Sigma}$ satisfies Eq. (41). We address the classification based on the method of the Clifford algebra^{147,164}. The specific procedure of the classification is summarized in Sec. IV B 2. In the next section, we discuss the classification results.

1. Classification results

Classification results of d_{EP} -dimensional exceptional band touching for $H_{\text{eff}}(\omega = 0, \mathbf{k})$ are summarized in Table II. Here, we consider the d -dimensional BZ.

For each case of $\delta = d - d_{\text{EP}}$ and symmetry class, this table elucidates the presence/absence of the $\delta - 1$ dimensional topological invariant in the BZ; “ \mathbb{Z} ” (“ \mathbb{Z}_2 ”) indicates the presence of a topological invariant taking an arbitrary integer (0 or 1), respectively; “0” appearing as the classification result (i.e., from sixth to 13-th column) indicates the absence of such topological invariants.

These classification results explain the exceptional band touching reported so far. For instance, this table indicates the \mathbb{Z} classification for class A with $\delta = 2$, meaning that there exists exceptional band touching characterized by a one-dimensional topological invariant. This classification result explains the presence of EPs observed in Fig. 3(b) ($d = 2$ and $d_{\text{EP}} = 0$). We note that the emergence of EPs for class A is also reported for systems with disorder^{58,61} or electron-phonon coupling⁵⁷. With $d = 3$ and $d_{\text{EP}} = 1$, we obtain the same δ , resulting in the \mathbb{Z} classification for class A. This fact also explains the emergence of exceptional loops in three-dimensional systems⁶⁴. The classification results for symmetry classes AI, AII, D, and C elucidate the stability of these band touching points in the presence/absence of PT - or CP -symmetry.

The emergence of SPERs observed in Fig. 8 is also consistent with Table II ($d = 2$ and $d_{\text{EP}} = 1$). For class AIII with $\delta = 1$, we obtain the \mathbb{Z} classification, implying the presence of the zero-th Chern number. The \mathbb{Z} classification for class AIII with $\delta = 1$ is also consistent with the emergence of SPESs observed in Fig. 10(c) ($d = 3$ and $d_{\text{EP}} = 2$). We note that the classification results for symmetry classes BDI, DIII, CII, and CI elucidate the stability of the exceptional band touching in the presence of PT - or CP -symmetry.

While we have mainly analyzed exceptional band touching for symmetry class A or AIII in the previous sections, the classification results summarized in Table II imply the existence of novel exceptional band touching. The verification of exceptional band touching for other cases of symmetry is still missing as well as the material realization.

It is also worth noting that the above table may explain the exceptional band touching away from $\omega = 0$ for class A by recognizing the frequency as an additional momentum, although we have restricted ourselves to $\omega = 0$ so far. Indeed, the emergence of exceptional rings in the ω - \mathbf{k} space has been demonstrated for two-dimensional heavy fermions⁶³ ($d = 3$ and $d_{\text{EP}} = 1$), which is consistent with the \mathbb{Z} classification for symmetry class A with $\delta = 2$. The above fact allows us to interpret the \mathbb{Z} classification for class A with $\delta = 4$; it implies the presence of novel EPs in the ω - \mathbf{k} space for three spatial dimensions. Further analysis in this direction should be addressed.

2. Details of the classification for the Hermitian Hamiltonian

As discussed in the beginning of this section, classification of the d_{EP} -dimensional exceptional band touching in d spatial dimensions is accomplished by classifying the $\delta - 1$ -dimensional gapped Hermitian Hamiltonian with additional chiral symmetry satisfying Eq. (41). Here, δ denotes codimension ($\delta = d - d_{\text{EP}}$). In this section, we address the classification of the gapped Hermitian Hamiltonian based on the method of the Clifford algebra^{147,164}.

In what follows are technical details of the derivation of Table II. Thus, readers, who are interested in physical interpretation of the classification results rather than the technical details, can skip this section.

Specifically, the topological classification based on the Clifford algebra can be carried out by the following steps^{147,164}.

(i) Deform the Hermitian Hamiltonian \tilde{H} to the Hermitian Dirac Hamiltonian H_0

$$H_0(\mathbf{k}) = \sum_{j=1, \dots, \delta-1} k_j \gamma_j + m \gamma_0, \quad (42)$$

where γ 's satisfy $\{\gamma_i, \gamma_j\} = 2\delta_{i,j}$ for $i, j = 0, \dots, \delta - 1$. Because such deformation is possible for an arbitrary gapped Hamiltonian, the problem is reduced to classifying the possible mass term γ_0 .

(ii) Consider a Clifford algebra Cl_q or $Cl_{p,q}$ with the matrices γ 's and the symmetry operators. Cl_q denotes the Clifford algebra composed of q generators,

$$\{e_1, e_2, \dots, e_q\}, \quad (43)$$

symmetry class	PT	CP	Γ	homotopy	$\delta = 1$	2	3	4	5	6	7	8	Clifford generators
A	0	0	0	$\pi_0(C_\delta)$	0	\mathbb{Z}	0	\mathbb{Z}	0	\mathbb{Z}	0	\mathbb{Z}	$\{\gamma_0, \dots, \gamma_{\delta-1}, \tilde{\Sigma}\}$
AIII	0	0	1	$\pi_0(C_{\delta+1})$	\mathbb{Z}	0	\mathbb{Z}	0	\mathbb{Z}	0	\mathbb{Z}	0	$\{\gamma_0, \dots, \gamma_{\delta-1}, \tilde{\Gamma}, \tilde{\Sigma}\}$
AI	1	0	0	$\pi_0(R_{\delta+6})$	0	\mathbb{Z}	\mathbb{Z}_2	\mathbb{Z}_2	0	\mathbb{Z}	0	0	$\{J\gamma_0, J\gamma_1, \dots, J\gamma_{\delta-1}, \widetilde{PT}, \widetilde{JPT}, \tilde{\Sigma}\}$
BDI	1	1	1	$\pi_0(R_{\delta+7})$	\mathbb{Z}	\mathbb{Z}_2	\mathbb{Z}_2	0	\mathbb{Z}	0	0	0	$\{J\gamma_0, J\gamma_1, \dots, J\gamma_{\delta-1}, J\tilde{\Gamma}, \widetilde{PT}, \widetilde{JPT}, \tilde{\Sigma}\}$
D	0	1	0	$\pi_0(R_\delta)$	\mathbb{Z}_2	\mathbb{Z}_2	0	\mathbb{Z}	0	0	0	\mathbb{Z}	$\{J\tilde{\Sigma}; \gamma_0, \gamma_1, \dots, \gamma_{\delta-1}, \widetilde{CP}, \widetilde{JCP}\}$
DIII	-1	1	1	$\pi_0(R_{\delta+1})$	\mathbb{Z}_2	0	\mathbb{Z}	0	0	0	\mathbb{Z}	\mathbb{Z}_2	$\{J\gamma_0, J\gamma_1, \dots, J\gamma_{\delta-1}, \widetilde{PT}, \widetilde{JPT}; J\tilde{\Gamma}, \tilde{\Sigma}\}$
AII	-1	0	0	$\pi_0(R_{\delta+2})$	0	\mathbb{Z}	0	0	0	\mathbb{Z}	\mathbb{Z}_2	\mathbb{Z}_2	$\{J\gamma_0, J\gamma_1, \dots, J\gamma_{\delta-1}, \widetilde{PT}, \widetilde{JPT}; \tilde{\Sigma}\}$
CII	-1	-1	1	$\pi_0(R_{\delta+3})$	\mathbb{Z}	0	0	0	\mathbb{Z}	\mathbb{Z}_2	\mathbb{Z}_2	0	$\{J\gamma_0, J\gamma_1, \dots, J\gamma_{\delta-1}, \widetilde{PT}, \widetilde{JPT}, J\tilde{\Gamma}; \tilde{\Sigma}\}$
C	0	-1	0	$\pi_0(R_{\delta+4})$	0	0	0	\mathbb{Z}	\mathbb{Z}_2	\mathbb{Z}_2	0	\mathbb{Z}	$\{\widetilde{CP}, \widetilde{JCP}, J\tilde{\Sigma}; \gamma_0, \gamma_1, \dots, \gamma_{\delta-1}\}$
CI	1	-1	1	$\pi_0(R_{\delta+5})$	0	0	\mathbb{Z}	\mathbb{Z}_2	\mathbb{Z}_2	0	\mathbb{Z}	0	$\{J\gamma_0, J\gamma_1, \dots, J\gamma_{\delta-1}, \widetilde{PT}, \widetilde{JPT}, J\tilde{\Gamma}, \tilde{\Sigma}\}$

TABLE II. Classification results of the d_{EP} -dimensional exceptional band touching for the d -dimensional non-Hermitian Hamiltonian $H_{\text{eff}}(\omega = 0, \mathbf{k})$. Here $\delta := d - d_{\text{EP}}$ denotes the codimension. The second, third, and fourth columns specify the symmetry class where ± 1 in the second (third) column indicates the sign of $\widetilde{PT}^2 = \pm 1$ ($\widetilde{CP}^2 = \pm 1$), respectively. Here, “0” in these columns indicates the absence of the corresponding symmetry. For a given δ , \mathbb{Z} (\mathbb{Z}_2) classification indicates the presence of $\delta - 1$ -dimensional topological invariant taking an arbitrary integer (0 or 1), respectively. “0” in these columns indicates the absence of such topological invariants. The homotopy of the classifying space C_q or R_q is shown in the fifth column. The classifying space can be obtained by considering the extension problem where the relevant generators of the Clifford algebra are shown in the last column (see Sec. IV B 2). Here, we assume that $[\widetilde{PT}, \widetilde{CP}] = 0$ which is satisfied with a proper choice of the gauge. $\tilde{\Gamma}$ for class BDI, DIII, CII, and CI is defined as the product of \widetilde{PT} and \widetilde{CP} with the prefactor satisfying $\tilde{\Gamma}^2 = \mathbb{1}$.

where the generator e_i satisfies $e_i^2 = 1$ for $i = 1, \dots, q$. $Cl_{p,q}$ represents the Clifford algebra composed of $p + q$ generators,

$$\{e_1, e_2, \dots, e_p; e_{p+1}, \dots, e_{p+q}\}, \quad (44)$$

where the generator e_i satisfies $e_i^2 = -1$ ($e_i^2 = 1$) for $i = 1, \dots, p$ ($i = p + 1, \dots, p + q$), respectively. We note that an operator J , satisfying $\{\widetilde{PT}, J\} = \{\widetilde{CP}, J\} = [H_0(\mathbf{k}), J] = 0$, needs to be introduced in the presence of PT - or CP -symmetry. This is because \widetilde{PT} and \widetilde{CP} are anti-unitary operators.

(iii) By adding the mass term γ_0 , consider the extension problem to obtain the corresponding classifying space which turns out to be C_q (R_{q-p}) when the extension problem is $Cl_q \rightarrow Cl_{q+1}$ ($Cl_{p,q} \rightarrow Cl_{p,q+1}$), respectively. Here, we note that the corresponding classifying space of the extension problem $Cl_{p,q} \rightarrow Cl_{p+1,q}$ is R_{2+p-q} ¹⁶⁴.

(iv) By making use of the relation summarized in Table III, obtain the classification result $\pi_0(C_q)$ [$\pi_0(R_q)$]. We note that the relations $\pi_0(C_{q+2}) = \pi_0(C_q)$ and $\pi_0(R_{q+8}) = \pi_0(R_q)$ hold, which are known as the Bott periodicity.

With the above procedure, (i)-(iv), we can obtain the classification results shown in Table II. In the last column, the Clifford algebra, which is generated by the mass term, the kinetic terms and symmetry operators, is shown for each symmetry class. Although one can reproduce the classification results from the last column, we explicitly apply the above procedure for class A and AII as examples.

class A- Remembering that the Hamiltonian \tilde{H} in $\delta - 1$ dimensions is chiral symmetric $\{\tilde{H}, \tilde{\Sigma}\} = 0$, we obtain the Clifford algebra C_δ generated by

$$\{\gamma_1, \dots, \gamma_{\delta-1}, \tilde{\Sigma}\}. \quad (45)$$

Introducing the mass term γ_0 results in the extension problem which is written as $Cl_\delta \rightarrow Cl_{\delta+1}$. Here, the Clifford algebra $Cl_{\delta+1}$ is generated by

$$\{\gamma_0, \gamma_1, \dots, \gamma_{\delta-1}, \tilde{\Sigma}\}, \quad (46)$$

which is shown in the last column of Table II. Therefore, the corresponding classifying space is C_δ , which indicates that the classification result is computed with $\pi_0(C_\delta)$. By making use of the Bott periodicity and the relation summarized in Table III, we obtain the classification results for $\delta = 1, \dots, 8$.

class AII- Firstly, we note that $\widetilde{PT}^2 = -1$ holds. Remembering that the Hamiltonian \tilde{H} in $\delta - 1$ dimensions is chiral symmetric $\{\tilde{H}, \tilde{\Sigma}\} = 0$, we obtain the Clifford algebra C_δ generated by

$$\{J\gamma_1, \dots, J\gamma_{\delta-1}, \widetilde{PT}, \widetilde{JPT}; \tilde{\Sigma}\}. \quad (47)$$

Introducing the mass term γ_0 results in the extension problem which is written as $Cl_{\delta+1,1} \rightarrow Cl_{\delta+2,1}$. Here, the Clifford algebra $Cl_{\delta+2,1}$ is generated by

$$\{J\gamma_0, J\gamma_1, \dots, J\gamma_{\delta-1}, \widetilde{PT}, \widetilde{JPT}, \widetilde{\Sigma}\}, \quad (48)$$

which is shown in the last column of Table II. Therefore, the corresponding classifying space is $R_{2+\delta}$, which indicates that the classification result is computed with $\pi_0(R_{2+\delta})$. By making use of the Bott periodicity and the relation summarized in Table III, we obtain the classification results for $\delta = 1, \dots, 8$.

classifying space	C_0	C_1	R_0	R_1	R_2	R_3	R_4	R_5	R_6	R_7
$\pi_0(C_q)$ or $\pi_0(R_q)$	\mathbb{Z}	0	\mathbb{Z}	\mathbb{Z}_2	\mathbb{Z}_2	0	\mathbb{Z}_2	0	0	0

TABLE III. Classifying space (C_q and R_q) and the corresponding homotopy group [$\pi_0(C_q)$ and $\pi_0(R_q)$].

We note that for $\delta = d + 1$, Table II indicates the classification results for the d -dimensional gapped Hamiltonian with additional chiral symmetry satisfying Eq. (41). In this case, the classification results are given by the homotopy group $\pi_0(C_{q-1+d})$ or $\pi_0(C_{q-1+d})$ with an integer q while the original ten-fold way classification for topological insulators/superconductors is given by $\pi_0(C_{q-d})$ or $\pi_0(C_{q-d})$. This is due to the fact that applying \widetilde{PT} or \widetilde{CP} does not flip the momentum $\mathbf{k}^{160,165,166}$ while applying time-reversal or particle-hole operator does ($\mathbf{k} \rightarrow -\mathbf{k}$).

V. SUMMARY AND OUTLOOK

In this paper, we have briefly reviewed the recently developed non-Hermitian perspective of the band structure in equilibrium systems. We have seen that the finite lifetime of quasi-particles induces EPs. In addition, we have seen that the symmetry of the many-body Hamiltonian results in SPERs (SPESs) in two (three) dimensions, respectively. While the above non-Hermitian perspective has been developed recently, there are several open questions to be addressed.

For instance, effects of EPs on transport properties should be further analyzed. As seen in this paper, the exceptional band touching induces low energy excitations such as Fermi arcs. The emergence of these low energy excitations may change the conductivity or other electromagnetic responses.

The experimental observation of EPs in electronic systems is also a crucial issue along this direction. Topological Kondo insulators such as $\text{SmB}_6^{167-173}$ and $\text{YbB}_{12}^{174,175}$ might serve as a platform of the EPs because they are strongly correlated materials and show Dirac cones at surfaces. Prior to the experimental observation, the quantitative analysis such as LDA+DMFT calculations should be carried out as well as the theoretical proposal of how to experimentally observe the EPs.

While this paper focuses on exceptional band touching, non-Hermiticity induces richer topological physics. Non-Hermitian skin effect is the another representative unique phenomenon^{77,82-86,176-179}; the energy spectrum of a non-Hermitian matrix significantly depends on the boundary condition when the skin effect occurs. Elucidating whether the non-Hermiticity by the finite lifetimes induces the skin effect is an intriguing theoretical open question to be addressed.

Finally, we comment on another significant issue of non-Hermiticity and correlations. Recently, a fractional quantum Hall phase, a topologically ordered phase, has been extended to non-Hermitian systems¹¹⁴. The extension of topologically ordered phases to non-Hermitian systems is further addressed for a non-Hermitian toric code^{180,181}. Developing the effective field theory to describe these non-Hermitian topologically ordered phases should be addressed as well as extending them to systems with symmetry (e.g., time-reversal symmetry).

VI. ACKNOWLEDGEMENTS

This work is partly supported by JSPS KAKENHI Grants No. JP15H05855, No. JP16K13845, No. JP17H06138, No. JP18H01140, No. JP18H04316, No. JP18K03511, No. JP18H05842, No. JP19K21032, and No. JP19H01838 and by JST CREST Grant No. JPMJCR19T1. A part of numerical data plotted in this paper were obtained on the

supercomputer at the ISSP in the University of Tokyo.

-
- ¹ Y. Hatsugai, Phys. Rev. Lett. **71**, 3697 (1993).
 - ² C. L. Kane and E. J. Mele, Phys. Rev. Lett. **95**, 146802 (2005).
 - ³ C. L. Kane and E. J. Mele, Phys. Rev. Lett. **95**, 226801 (2005).
 - ⁴ B. A. Bernevig, T. L. Hughes, and S.-C. Zhang, **314**, 1757 (2006).
 - ⁵ X.-L. Qi, T. L. Hughes, and S.-C. Zhang, Phys. Rev. B **78**, 195424 (2008).
 - ⁶ M. Z. Hasan and C. L. Kane, Rev. Mod. Phys. **82**, 3045 (2010).
 - ⁷ X.-L. Qi and S.-C. Zhang, Rev. Mod. Phys. **83**, 1057 (2011).
 - ⁸ X. Wan, A. M. Turner, A. Vishwanath, and S. Y. Savrasov, Phys. Rev. B **83**, 205101 (2011).
 - ⁹ H. Weng, C. Fang, Z. Fang, B. A. Bernevig, and X. Dai, Phys. Rev. X **5**, 011029 (2015).
 - ¹⁰ S.-Y. Xu, I. Belopolski, N. Alidoust, M. Neupane, G. Bian, C. Zhang, R. Sankar, G. Chang, Z. Yuan, C.-C. Lee, S.-M. Huang, H. Zheng, J. Ma, D. S. Sanchez, B. Wang, A. Bansil, F. Chou, P. P. Shibayev, H. Lin, S. Jia, and M. Z. Hasan, **349**, 613 (2015).
 - ¹¹ B. Q. Lv, H. M. Weng, B. B. Fu, X. P. Wang, H. Miao, J. Ma, P. Richard, X. C. Huang, L. X. Zhao, G. F. Chen, Z. Fang, X. Dai, T. Qian, and H. Ding, Phys. Rev. X **5**, 031013 (2015).
 - ¹² S. Ryu and Y. Hatsugai, Phys. Rev. Lett. **89**, 077002 (2002).
 - ¹³ S. Raghu, X.-L. Qi, C. Honerkamp, and S.-C. Zhang, Phys. Rev. Lett. **100**, 156401 (2008).
 - ¹⁴ R. S. K. Mong, A. M. Essin, and J. E. Moore, Phys. Rev. B **81**, 245209 (2010).
 - ¹⁵ M. Hohenadler, T. C. Lang, and F. F. Assaad, Phys. Rev. Lett. **106**, 100403 (2011).
 - ¹⁶ Y. Yamaji and M. Imada, Phys. Rev. B **83**, 205122 (2011).
 - ¹⁷ S.-L. Yu, X. C. Xie, and J.-X. Li, Phys. Rev. Lett. **107**, 010401 (2011).
 - ¹⁸ T. Yoshida, S. Fujimoto, and N. Kawakami, Phys. Rev. B **85**, 125113 (2012).
 - ¹⁹ Y. Tada, R. Peters, M. Oshikawa, A. Koga, N. Kawakami, and S. Fujimoto, Phys. Rev. B **85**, 165138 (2012).
 - ²⁰ V. Gurarie, Phys. Rev. B **83**, 085426 (2011).
 - ²¹ A. M. Essin and V. Gurarie, Phys. Rev. B **84**, 125132 (2011).
 - ²² M. Hohenadler and F. F. Assaad, Journal of Physics: Condensed Matter **25**, 143201 (2013).
 - ²³ S. Rachel, Reports on Progress in Physics **81**, 116501 (2018).
 - ²⁴ D. C. Tsui, H. L. Stormer, and A. C. Gossard, Phys. Rev. Lett. **48**, 1559 (1982).
 - ²⁵ R. B. Laughlin, Phys. Rev. Lett. **50**, 1395 (1983).
 - ²⁶ J. K. Jain, Phys. Rev. Lett. **63**, 199 (1989).
 - ²⁷ X.-G. Wen, Advances in Physics **44**, 405 (1995).
 - ²⁸ A. Kitaev, Annals of Physics **303**, 2 (2003).
 - ²⁹ A. Hamma, P. Zanardi, and X.-G. Wen, Phys. Rev. B **72**, 035307 (2005).
 - ³⁰ A. Kitaev, Annals of Physics **321**, 2 (2006), January Special Issue.
 - ³¹ E. Tang, J.-W. Mei, and X.-G. Wen, Phys. Rev. Lett. **106**, 236802 (2011).
 - ³² K. Sun, Z. Gu, H. Katsura, and S. Das Sarma, Phys. Rev. Lett. **106**, 236803 (2011).
 - ³³ T. Neupert, L. Santos, C. Chamon, and C. Mudry, Phys. Rev. Lett. **106**, 236804 (2011).
 - ³⁴ N. Regnault and B. A. Bernevig, Phys. Rev. X **1**, 021014 (2011).
 - ³⁵ D. N. Sheng, Z.-C. Gu, K. Sun, and L. Sheng, Nature Communications **2**, 389 EP (2011), article.
 - ³⁶ E. J. Bergholtz and Z. Liu, International Journal of Modern Physics B **27**, 1330017 (2013).
 - ³⁷ D. Pesin and L. Balents, Nature Physics **6**, 376 EP (2010), article.
 - ³⁸ S. R. Manmana, A. M. Essin, R. M. Noack, and V. Gurarie, Phys. Rev. B **86**, 205119 (2012).
 - ³⁹ T. Yoshida, R. Peters, S. Fujimoto, and N. Kawakami, Phys. Rev. Lett. **112**, 196404 (2014).
 - ⁴⁰ T. Yoshida and N. Kawakami, Phys. Rev. B **94**, 085149 (2016).
 - ⁴¹ K. Kudo, T. Yoshida, and Y. Hatsugai, Phys. Rev. Lett. **123**, 196402 (2019).
 - ⁴² L. Fidkowski and A. Kitaev, Phys. Rev. B **81**, 134509 (2010).
 - ⁴³ L. Fidkowski and A. Kitaev, Phys. Rev. B **83**, 075103 (2011).
 - ⁴⁴ A. M. Turner, F. Pollmann, and E. Berg, Phys. Rev. B **83**, 075102 (2011).
 - ⁴⁵ S. Ryu and S.-C. Zhang, Phys. Rev. B **85**, 245132 (2012).
 - ⁴⁶ H. Yao and S. Ryu, Phys. Rev. B **88**, 064507 (2013).
 - ⁴⁷ X.-L. Qi, New J. Phys. **15**, 065002 (2013).
 - ⁴⁸ Y.-M. Lu and A. Vishwanath, Phys. Rev. B **86**, 125119 (2012).
 - ⁴⁹ M. Levin and A. Stern, Phys. Rev. B **86**, 115131 (2012).
 - ⁵⁰ C.-T. Hsieh, T. Morimoto, and S. Ryu, Phys. Rev. B **90**, 245111 (2014).
 - ⁵¹ C. Wang, A. C. Potter, and T. Senthil, Science **343**, 629 (2014).
 - ⁵² H. Isobe and L. Fu, Phys. Rev. B **92**, 081304 (2015).
 - ⁵³ T. Yoshida and A. Furusaki, Phys. Rev. B **92**, 085114 (2015).
 - ⁵⁴ T. Morimoto, A. Furusaki, and C. Mudry, Phys. Rev. B **92**, 125104 (2015).
 - ⁵⁵ T. Yoshida, A. Daido, Y. Yanase, and N. Kawakami, Phys. Rev. Lett. **118**, 147001 (2017).

- ⁵⁶ T. Yoshida, I. Danshita, R. Peters, and N. Kawakami, Phys. Rev. Lett. **121**, 025301 (2018).
- ⁵⁷ V. Kozii and L. Fu, arXiv preprint arXiv:1708.05841 (2017).
- ⁵⁸ A. A. Zyuzin and A. Y. Zyuzin, Phys. Rev. B **97**, 041203 (2018).
- ⁵⁹ T. Yoshida, R. Peters, and N. Kawakami, Phys. Rev. B **98**, 035141 (2018).
- ⁶⁰ T. Yoshida, R. Peters, N. Kawakami, and Y. Hatsugai, Phys. Rev. B **99**, 121101 (2019).
- ⁶¹ M. Papaj, H. Isobe, and L. Fu, Phys. Rev. B **99**, 201107 (2019).
- ⁶² K. Kimura, T. Yoshida, and N. Kawakami, Phys. Rev. B **100**, 115124 (2019).
- ⁶³ Y. Michishita, T. Yoshida, and R. Peters, arXiv preprint arXiv:1905.12287 (2019).
- ⁶⁴ T. Matsushita, Y. Nagai, and S. Fujimoto, Phys. Rev. B **100**, 245205 (2019).
- ⁶⁵ N. Hatano and D. R. Nelson, Phys. Rev. Lett. **77**, 570 (1996).
- ⁶⁶ N. Hatano and D. R. Nelson, Phys. Rev. B **58**, 8384 (1998).
- ⁶⁷ C. M. Bender and S. Boettcher, Phys. Rev. Lett. **80**, 5243 (1998).
- ⁶⁸ C. M. Bender, S. Boettcher, and P. N. Meisinger, Journal of Mathematical Physics **40**, 2201 (1999).
- ⁶⁹ K. Esaki, M. Sato, K. Hasebe, and M. Kohmoto, Phys. Rev. B **84**, 205128 (2011).
- ⁷⁰ M. Sato, K. Hasebe, K. Esaki, and M. Kohmoto, Progress of Theoretical Physics **127**, 937 (2012).
- ⁷¹ T. Fukui and N. Kawakami, Phys. Rev. B **58**, 16051 (1998).
- ⁷² T. E. Lee, Phys. Rev. Lett. **116**, 133903 (2016).
- ⁷³ T. Katō, *Perturbation theory for linear operators*, Vol. 132 (Springer, 1966).
- ⁷⁴ H. Shen, B. Zhen, and L. Fu, arXiv preprint arXiv:1706.07435 (2017).
- ⁷⁵ Y. Xu, S.-T. Wang, and L.-M. Duan, Phys. Rev. Lett. **118**, 045701 (2017).
- ⁷⁶ J. Carlström, M. Stålhammar, J. C. Budich, and E. J. Bergholtz, Phys. Rev. B **99**, 161115 (2019).
- ⁷⁷ S. Yao and Z. Wang, Phys. Rev. Lett. **121**, 086803 (2018).
- ⁷⁸ F. K. Kunst, E. Edvardsson, J. C. Budich, and E. J. Bergholtz, Phys. Rev. Lett. **121**, 026808 (2018).
- ⁷⁹ E. Edvardsson, F. K. Kunst, and E. J. Bergholtz, Phys. Rev. B **99**, 081302 (2019).
- ⁸⁰ K. Yokomizo and S. Murakami, Phys. Rev. Lett. **123**, 066404 (2019).
- ⁸¹ N. Okuma and M. Sato, Phys. Rev. Lett. **123**, 097701 (2019).
- ⁸² L. Xiao, T. Deng, K. Wang, G. Zhu, Z. Wang, W. Yi, and P. Xue, arXiv preprint arXiv:1907.12566 (2019).
- ⁸³ V. M. Martinez Alvarez, J. E. Barrios Vargas, and L. E. F. Foa Torres, Phys. Rev. B **97**, 121401 (2018).
- ⁸⁴ C. H. Lee and R. Thomale, Phys. Rev. B **99**, 201103 (2019).
- ⁸⁵ K. Zhang, Z. Yang, and C. Fang, arXiv preprint arXiv:1910.01131 (2019).
- ⁸⁶ N. Okuma, K. Kawabata, K. Shiozaki, and M. Sato, arXiv preprint arXiv:1910.02878 (2019).
- ⁸⁷ Z. Gong, Y. Ashida, K. Kawabata, K. Takasan, S. Higashikawa, and M. Ueda, Phys. Rev. X **8**, 031079 (2018).
- ⁸⁸ K. Kawabata, S. Higashikawa, Z. Gong, Y. Ashida, and M. Ueda, Nature Communications **10**, 297 (2019).
- ⁸⁹ K. Kawabata, K. Shiozaki, M. Ueda, and M. Sato, Phys. Rev. X **9**, 041015 (2019).
- ⁹⁰ H. Zhou and J. Y. Lee, Phys. Rev. B **99**, 235112 (2019).
- ⁹¹ J. C. Budich, J. Carlström, F. K. Kunst, and E. J. Bergholtz, Phys. Rev. B **99**, 041406 (2019).
- ⁹² R. Okugawa and T. Yokoyama, Phys. Rev. B **99**, 041202 (2019).
- ⁹³ H. Zhou, J. Y. Lee, S. Liu, and B. Zhen, Optica **6**, 190 (2019).
- ⁹⁴ K. Kawabata, T. Bessho, and M. Sato, Phys. Rev. Lett. **123**, 066405 (2019).
- ⁹⁵ A. Ghatak, M. Brandenbourger, J. van Wezel, and C. Coulais, arXiv preprint arXiv:1907.11619 (2019).
- ⁹⁶ V. V. Colini Scheibner, William T. M. Irvine, arXiv preprint arXiv:2001.04969 (2020).
- ⁹⁷ P. A. McClarty and J. G. Rau, Phys. Rev. B **100**, 100405 (2019).
- ⁹⁸ E. J. Bergholtz and J. C. Budich, Phys. Rev. Research **1**, 012003 (2019).
- ⁹⁹ E. J. Bergholtz, J. C. Budich, and F. K. Kunst, arXiv preprint arXiv:1912.10048 (2019).
- ¹⁰⁰ A. Guo, G. J. Salamo, D. Duchesne, R. Morandotti, M. Volatier-Ravat, V. Aimez, G. A. Siviloglou, and D. N. Christodoulides, Phys. Rev. Lett. **103**, 093902 (2009).
- ¹⁰¹ C. E. Rüter, K. G. Makris, R. El-Ganainy, D. N. Christodoulides, M. Segev, and D. Kip, Nature physics **6**, 192 (2010).
- ¹⁰² A. Szameit, M. C. Rechtsman, O. Bahat-Treidel, and M. Segev, Phys. Rev. A **84**, 021806 (2011).
- ¹⁰³ A. Regensburger, C. Bersch, M.-A. Miri, G. Onishchukov, D. N. Christodoulides, and U. Peschel, Nature **488**, 167 (2012).
- ¹⁰⁴ B. Zhen, C. W. Hsu, Y. Igarashi, L. Lu, I. Kaminer, A. Pick, S.-L. Chua, J. D. Joannopoulos, and M. Soljacic, Nature **525**, 354 EP (2015).
- ¹⁰⁵ A. U. Hassan, B. Zhen, M. Soljačić, M. Khajavikhan, and D. N. Christodoulides, Phys. Rev. Lett. **118**, 093002 (2017).
- ¹⁰⁶ L. Feng, R. El-Ganainy, and L. Ge, Nature Photonics **11**, 752 (2017).
- ¹⁰⁷ K. Takata and M. Notomi, Phys. Rev. Lett. **121**, 213902 (2018).
- ¹⁰⁸ H. Zhou, C. Peng, Y. Yoon, C. W. Hsu, K. A. Nelson, L. Fu, J. D. Joannopoulos, M. Soljačić, and B. Zhen, **359**, 1009 (2018).
- ¹⁰⁹ K. Takata, K. Nozaki, E. Kuramochi, S. Matsuo, K. Takeda, T. Fujii, S. Kita, A. Shinya, and M. Notomi, in *Frontiers in Optics + Laser Science APS/DLS* (Optical Society of America, 2019) p. FM4E.3.
- ¹¹⁰ T. Ozawa, H. M. Price, A. Amo, N. Goldman, M. Hafezi, L. Lu, M. C. Rechtsman, D. Schuster, J. Simon, O. Zilberberg, and I. Carusotto, Rev. Mod. Phys. **91**, 015006 (2019).
- ¹¹¹ Z. Gong, S. Higashikawa, and M. Ueda, Phys. Rev. Lett. **118**, 200401 (2017).
- ¹¹² T. Liu, Y.-R. Zhang, Q. Ai, Z. Gong, K. Kawabata, M. Ueda, and F. Nori, Phys. Rev. Lett. **122**, 076801 (2019).
- ¹¹³ N. Hatano, Molecular Physics **117**, 2121 (2019).
- ¹¹⁴ T. Yoshida, K. Kudo, and Y. Hatsugai, Scientific Reports **9**, 16895 (2019).

- ¹¹⁵ Y. Ashida, S. Furukawa, and M. Ueda, Phys. Rev. A **94**, 053615 (2016).
¹¹⁶ Y. Ashida, S. Furukawa, and M. Ueda, Nature communications **8**, 15791 (2017).
¹¹⁷ M. Nakagawa, N. Kawakami, and M. Ueda, Phys. Rev. Lett. **121**, 203001 (2018).
¹¹⁸ K. Yamamoto, M. Nakagawa, K. Adachi, K. Takasan, M. Ueda, and N. Kawakami, arXiv preprint arXiv:1903.04720 (2019).
¹¹⁹ N. Shibata and H. Katsura, Phys. Rev. B **99**, 174303 (2019).
¹²⁰ F. Scazza, C. Hofrichter, M. H. Danfer, P. C. De Groot, I. Bloch, and S. F. Danling, Nature Physics **10**, 779 EP (2014), article.
¹²¹ G. Pagano, M. Mancini, G. Cappellini, L. Livì, C. Sias, J. Catani, M. Inguscio, and L. Fallani, Phys. Rev. Lett. **115**, 265301 (2015).
¹²² M. Höfer, L. Riegger, F. Scazza, C. Hofrichter, D. R. Fernandes, M. M. Parish, J. Levinsen, I. Bloch, and S. Fölling, Phys. Rev. Lett. **115**, 265302 (2015).
¹²³ L. Riegger, N. Darkwah Oppong, M. Höfer, D. R. Fernandes, I. Bloch, and S. Fölling, Phys. Rev. Lett. **120**, 143601 (2018).
¹²⁴ T. Tomita, S. Nakajima, I. Danshita, Y. Takasu, and Y. Takahashi, **3** (2017), 10.1126/sciadv.1701513.
¹²⁵ M. Horio, T. Adachi, Y. Mori, A. Takahashi, T. Yoshida, H. Suzuki, L. C. C. Ambolode, K. Okazaki, K. Ono, H. Kumigashira, H. Anzai, M. Arita, H. Namatame, M. Taniguchi, D. Ootsuki, K. Sawada, M. Takahashi, T. Mizokawa, Y. Koike, and A. Fujimori, Nature Communications **7**, 10567 (2016).
¹²⁶ B. S. Tan, Y.-T. Hsu, B. Zeng, M. C. Hatnean, N. Harrison, Z. Zhu, M. Hartstein, M. Kiourlappou, A. Srivastava, M. D. Johannes, T. P. Murphy, J.-H. Park, L. Balicas, G. G. Lonzarich, G. Balakrishnan, and S. E. Sebastian, **349**, 287 (2015).
¹²⁷ Z. Xiang, Y. Kasahara, T. Asaba, B. Lawson, C. Tinsman, L. Chen, K. Sugimoto, S. Kawaguchi, Y. Sato, G. Li, S. Yao, Y. L. Chen, F. Iga, J. Singleton, Y. Matsuda, and L. Li, **362**, 65 (2018).
¹²⁸ H. Liu, M. Hartstein, G. J. Wallace, A. J. Davies, M. C. Hatnean, M. D. Johannes, N. Shitsevalova, G. Balakrishnan, and S. E. Sebastian, Journal of Physics: Condensed Matter **30**, 16LT01 (2018).
¹²⁹ This can be seen as follows. Firstly, by diagonalizing the Hamiltonian, we rewrite the vorticity as

$$\nu = \frac{1}{4\pi i} \oint d\mathbf{k} \cdot \nabla_{\mathbf{k}} \sum_n \log[E_n(\mathbf{k}) - E_0],$$

where E_n ($n = 1, \dots, \dim H$) denotes the energy eigenvalues of H . Substituting Eq. (1) to the above equation, we obtain

$$\nu = \frac{1}{4\pi i} \oint d\mathbf{k} \cdot \nabla_{\mathbf{k}} \sum_{n=\pm} \log[E_n(\mathbf{k}) - E_0],$$

where E_{\pm} is the energy eigenvalues [see Eq. (2)]. This can be rewritten as

$$\begin{aligned} \nu &= \frac{1}{4\pi i} \oint d\mathbf{k} \cdot \nabla_{\mathbf{k}} [\log \Delta(\mathbf{k}) + \log \{-\Delta(\mathbf{k})\}] \\ &= \frac{1}{4\pi i} \oint d\mathbf{k} \cdot \nabla_{\mathbf{k}} [2 \log \Delta(\mathbf{k})] \\ &= \frac{1}{2\pi} \oint d\mathbf{k} \cdot \nabla_{\mathbf{k}} \arg(E_+ - E_-), \end{aligned}$$

with $\Delta := (E_+ - E_-)/2 = \sqrt{b^2 - d^2 + 2i\mathbf{b} \cdot \mathbf{d}}$. Here, we have omitted the term proportional to $b_0 + id_0$ by assuming that it is canceled with E_0 . The last line of the above equation corresponds to the right hand side of Eq. (6).

- ¹³⁰ Eq. (5) is obtained as follows. With $\Sigma = \mathbb{1} \otimes \rho_3$, Eq. (9) is rewritten as

$$\begin{aligned} \nu_W &= \frac{1}{4\pi i} \oint d^2\mathbf{k} \cdot \text{tr} \left[\begin{pmatrix} \mathbb{1} & \\ & -\mathbb{1} \end{pmatrix}_{\rho} \begin{pmatrix} 0 & H(\mathbf{k}) \\ H^\dagger(\mathbf{k}) & 0 \end{pmatrix}_{\rho}^{-1} \nabla_{\mathbf{k}} \begin{pmatrix} 0 & H(\mathbf{k}) \\ H^\dagger(\mathbf{k}) & 0 \end{pmatrix}_{\rho} \right] \\ &= \frac{1}{4\pi i} \oint d^2\mathbf{k} \cdot \text{tr} [\nabla_{\mathbf{k}} \log H^\dagger(\mathbf{k}) - \nabla_{\mathbf{k}} \log H(\mathbf{k})] \\ &= \frac{-1}{2\pi} \oint d^2\mathbf{k} \cdot \nabla_{\mathbf{k}} \log \det H(\mathbf{k}). \end{aligned}$$

The last line corresponds to Eq. (5) up to the prefactor; $\nu = -\nu_W/2$.

- ¹³¹ A. A. Abrikosov, L. P. Gorkov, and I. E. Dzyaloshinski, *Methods of quantum field theory in statistical physics* (Courier Corporation, 2012).
¹³² W. Metzner and D. Vollhardt, Phys. Rev. Lett. **62**, 324 (1989).
¹³³ E. Müller-Hartmann, Zeitschrift für Physik B Condensed Matter **74**, 507 (1989).
¹³⁴ A. Georges and G. Kotliar, Phys. Rev. B **45**, 6479 (1992).
¹³⁵ A. Georges, G. Kotliar, W. Krauth, and M. J. Rozenberg, Rev. Mod. Phys. **68**, 13 (1996).
¹³⁶ The action of the effective impurity model is written as

$$\begin{aligned} \mathcal{Z}_{\text{imp}} &= \int \prod_s \mathcal{D}\bar{c}_{bs} \mathcal{D}c_{bs} \text{tr}_S \exp(-\mathcal{S}_{\text{imp}}), \\ -\mathcal{S}_{\text{imp}} &= \int d\tau d\tau' \sum_s \bar{c}_{bs} \mathcal{G}_s^{-1}(\tau - \tau') c_{bs} - H_{\text{int}} \delta(\tau - \tau'), \end{aligned}$$

where H_{int} denotes the local interaction term $H_{\text{int}} := J\mathbf{s}_0 \cdot \mathbf{S}$. $\delta(\tau - \tau')$ is the delta function. tr_S denotes taking trace for the localized spin. $\mathcal{G}_s(\tau - \tau')$ denotes the Green's function of the effective bath. \bar{c}_{bs} (c_{bs}) is a Grassmannian variable which corresponds to the creation operator c_{0bs}^\dagger (annihilation operator c_{0bs}) at site $i = 0$. Solving the above model with an

impurity solver, we obtain the self-energy Σ_{bs} , which allows us to compute the Green's function as

$$\mathcal{G}_s^{-1}(i\omega_n) = \left[\frac{1}{N} \sum_{\mathbf{k}} \frac{1}{i\omega_n - h(\mathbf{k}) - \Sigma_s(i\omega_n)} \right] + \Sigma_s(i\omega_n),$$

with the Matsubara frequency $\omega_n = (2n+1)\pi T$. Here, N denotes the number of unit cells. Computing the effective Green's function \mathcal{G}_s^{-1} yields the self-energy $\Sigma_s(i\omega_n)$.

- ¹³⁷ K. G. Wilson, Rev. Mod. Phys. **47**, 773 (1975).
¹³⁸ R. Peters, T. Pruschke, and F. B. Anders, Phys. Rev. B **74**, 245114 (2006).
¹³⁹ R. Bulla, T. A. Costi, and T. Pruschke, Rev. Mod. Phys. **80**, 395 (2008).
¹⁴⁰ J. E. Hirsch and R. M. Fye, Phys. Rev. Lett. **56**, 2521 (1986).
¹⁴¹ P. Werner, A. Comanac, L. de' Medici, M. Troyer, and A. J. Millis, Phys. Rev. Lett. **97**, 076405 (2006).
¹⁴² P. Werner and A. J. Millis, Phys. Rev. B **74**, 155107 (2006).
¹⁴³ M. A. Ruderman and C. Kittel, Phys. Rev. **96**, 99 (1954).
¹⁴⁴ T. Kasuya, Progress of Theoretical Physics **16**, 45 (1956).
¹⁴⁵ K. Yosida, Phys. Rev. **106**, 893 (1957).
¹⁴⁶ A. P. Schnyder, S. Ryu, A. Furusaki, and A. W. W. Ludwig, Phys. Rev. B **78**, 195125 (2008).
¹⁴⁷ A. Kitaev, AIP Conf. Proc. **1134**, 22 (2009).
¹⁴⁸ S. Ryu, A. P. Schnyder, A. Furusaki, and A. W. W. Ludwig, New J. Phys. **12**, 065010 (2010).
¹⁴⁹ C.-K. Chiu, J. C. Y. Teo, A. P. Schnyder, and S. Ryu, Rev. Mod. Phys. **88**, 035005 (2016).
¹⁵⁰ R. Yamazaki, S. Taie, S. Sugawa, and Y. Takahashi, Phys. Rev. Lett. **105**, 050405 (2010).
¹⁵¹ L. W. Clark, L.-C. Ha, C.-Y. Xu, and C. Chin, Phys. Rev. Lett. **115**, 155301 (2015).

¹⁵² This fact can be understood as follows. Suppose that the Hamiltonian is chiral symmetric [see Eq. (20)]. Then, with the eigenvalue E_n and the right eigenvector $|\varphi_n^R\rangle$ ($H|\varphi_n^R\rangle = |\varphi_n^R\rangle E_n$, $n \in \mathbb{Z}$), we obtain the relation

$$H^\dagger U_\Gamma^\dagger |\varphi_n^R\rangle = -U_\Gamma^\dagger |\varphi_n^R\rangle E_n.$$

Here, we have used Eq. (20). Noticing that the eigenvalues problem of the left eigenvector $|\varphi_n^L\rangle$ ($n \in \mathbb{Z}$) is written as $H^\dagger |\varphi_n^L\rangle = |\varphi_n^L\rangle E_n^*$, we can see that the vector $U_\Gamma^\dagger |\varphi_n^R\rangle$ is the left eigenvector with the eigenvalue E_n .

- ¹⁵³ X. Y. Zhang, M. J. Rozenberg, and G. Kotliar, Phys. Rev. Lett. **70**, 1666 (1993).
¹⁵⁴ H. Kajueter and G. Kotliar, Phys. Rev. Lett. **77**, 131 (1996).

¹⁵⁵ The local magnetic susceptibility χ_α^s is computed as follows. With the RPA, the matrix of the susceptibility is written as $\chi^{\text{RPA}}(i\epsilon_n, \mathbf{q}) = (\mathbb{1} - \chi^0 U) \chi^0$,

with $U = \text{diag}(U_A, U_B)$ and ξ^0 defined as

$$\chi_{\alpha\beta}^0(i\epsilon_n, \mathbf{q}) = -\frac{T}{N} \sum_{\mathbf{k}, m} G_{\alpha\beta}(i\omega_m + i\epsilon_n, \mathbf{q} + \mathbf{k}) G_{\beta\alpha}(i\omega_n, \mathbf{k}).$$

Here, ω_n and ϵ_n denote the Matsubara frequency [$\omega_n = (2n+1)\pi T$ and $\epsilon_n = 2n\pi T$ with $n \in \mathbb{Z}$]. N denotes the number of unit cells. The local magnetic susceptibility χ_α^s is obtained as

$$\begin{aligned} \chi_A^s &= (\chi_{AA}^{\text{RPA}} + \chi_{AB}^{\text{RPA}})/2, \\ \chi_B^s &= (\chi_{BB}^{\text{RPA}} + \chi_{BA}^{\text{RPA}})/2, \end{aligned}$$

with $\mathbf{q} = 0$. We set $\epsilon_n \rightarrow 0$ instead of doing analytic continuation.

- ¹⁵⁶ Eq. (32a) can be obtained as follows. Firstly, we note that the following relations hold

$$\begin{aligned} it\hat{H} &= it\hat{U}_{PT}\hat{H}^*\hat{U}_{PT}^\dagger, \\ \hat{U}_{PT}^\dagger \hat{c}_{i\alpha}^\dagger \hat{U}_{PT} &= \sum_{\alpha'} \hat{c}_{-i\alpha'}^\dagger U_{\alpha\alpha'}^\dagger, \\ \langle n^* | \hat{A} | m^* \rangle &= \sum_{\{i\alpha\}, \{j\beta\}} \langle n^* | \{i\alpha\} \rangle \langle \{i\alpha\} | \hat{A} | \{j\beta\} \rangle \langle \{j\beta\} | m^* \rangle \\ &= \sum_{\{i\alpha\}, \{j\beta\}} \langle m | \{j\beta\} \rangle \langle \{j\beta\} | \hat{A}^T | \{i\alpha\} \rangle \langle \{i\alpha\} | n \rangle \\ &= \langle m | \hat{A}^T | n \rangle, \end{aligned}$$

where $|\{i\alpha\}\rangle$ and $|\{j\beta\}\rangle$ denote the states generated by applying the creation operators $\hat{c}_{i\alpha}^\dagger$ on the vacuum $|0\rangle$. $|n\rangle$ and $|m\rangle$ are arbitrary states. $|n^*\rangle := \sum_{\{i\alpha\}} |\{i\alpha\}\rangle \langle n | \{i\alpha\} \rangle$. By using the above relations, the correlation function $\langle \hat{c}_{i\alpha}(t) \hat{c}_{j\gamma}^\dagger \rangle$ is rewritten as

$$\begin{aligned} \langle \hat{c}_{i\alpha}(t) \hat{c}_{j\gamma}^\dagger \rangle &= Z^{-1} \text{tr}[e^{-\beta\hat{H}} e^{it\hat{H}} \hat{c}_{i\alpha} e^{-it\hat{H}} \hat{c}_{j\gamma}^\dagger] \\ &= Z^{-1} \text{tr}[e^{-\beta\hat{H}^*} e^{it\hat{H}^*} \hat{U}_{PT}^\dagger \hat{c}_{i\alpha} \hat{U}_{PT} e^{-it\hat{H}^*} \hat{U}_{PT}^\dagger \hat{c}_{j\gamma}^\dagger \hat{U}_{PT}] \\ &= Z^{-1} \sum_{\alpha'\gamma'} \text{tr}[e^{-\beta\hat{H}^*} e^{it\hat{H}^*} U_{PT, \alpha\alpha'} \hat{c}_{-i\alpha'} e^{-it\hat{H}^*} \hat{c}_{-j\gamma'}^\dagger U_{PT, \gamma'\gamma}^\dagger] \\ &= Z^{-1} \sum_{\alpha'\gamma'} U_{PT, \alpha\alpha'} U_{PT, \gamma'\gamma}^\dagger \text{tr}[\hat{c}_{-j\gamma'} e^{-it\hat{H}} \hat{c}_{-i\alpha'}^\dagger e^{it\hat{H}} e^{-\beta\hat{H}}] \\ &= \sum_{\alpha'\gamma'} U_{PT, \alpha\alpha'} U_{PT, \gamma'\gamma}^\dagger \langle \hat{c}_{-j\gamma'}(t) \hat{c}_{-i\alpha'}^\dagger \rangle, \end{aligned}$$

which is equivalent to

$$\langle \hat{c}_{\mathbf{k}\alpha}(t) \hat{c}_{\mathbf{k}\gamma}^\dagger \rangle = \sum_{\alpha'\gamma'} U_{PT,\alpha\alpha'} U_{PT,\gamma'\gamma}^\dagger \langle \hat{c}_{\mathbf{k}\gamma'}(t) \hat{c}_{\mathbf{k}\alpha'}^\dagger \rangle.$$

Here, Z denotes the partition function. In a similar way, we obtain

$$\langle \hat{c}_{\mathbf{k}\gamma}^\dagger \hat{c}_{\mathbf{k}\alpha}(t) \rangle = \sum_{\alpha'\gamma'} U_{PT,\alpha\alpha'} U_{PT,\gamma'\gamma}^\dagger \langle \hat{c}_{\mathbf{k}\alpha'}^\dagger \hat{c}_{\mathbf{k}\gamma'}(t) \rangle.$$

Remembering that the definition of the retarded Green's function [see Eq. (10)], we end up with Eq. (32a).

¹⁵⁷ Eq. (35) can be obtained by the following calculations. Firstly, we note that the following relation holds.

$$\hat{U}_{CP}^\dagger \hat{c}_{i\alpha}^\dagger \hat{U}_{CP} = \sum_{\alpha'} \hat{c}_{-i\alpha'} U_{\alpha'\alpha}^\dagger.$$

By using the above relations, $\langle \hat{c}_{i\alpha}(t) \hat{c}_{j\gamma}^\dagger \rangle$ is rewritten as

$$\begin{aligned} \langle \hat{c}_{i\alpha}(t) \hat{c}_{j\gamma}^\dagger \rangle &= Z^{-1} \text{tr}[e^{-\beta \hat{H}} e^{it\hat{H}} \hat{c}_{i\alpha} e^{-it\hat{H}} \hat{c}_{j\gamma}^\dagger] \\ &= Z^{-1} \text{tr}[e^{-\beta \hat{U}_{CP} \hat{H} \hat{U}_{CP}^\dagger} e^{it\hat{U}_{CP} \hat{H} \hat{U}_{CP}^\dagger} \hat{c}_{i\alpha} e^{-it\hat{U}_{CP} \hat{H} \hat{U}_{CP}^\dagger} \hat{c}_{j\gamma}^\dagger] \\ &= Z^{-1} \text{tr}[e^{-\beta \hat{H}} e^{it\hat{H}} \hat{U}_{CP}^\dagger \hat{c}_{i\alpha} \hat{U}_{CP} e^{-it\hat{H}} \hat{U}_{CP}^\dagger \hat{c}_{j\gamma}^\dagger \hat{U}_{CP}] \\ &= Z^{-1} \sum_{\alpha'\gamma'} \text{tr}[e^{-\beta \hat{H}} e^{it\hat{H}} U_{CP,\alpha\alpha'} \hat{c}_{-i\alpha'}^\dagger e^{-it\hat{H}} \hat{c}_{-j\gamma'} U_{CP,\gamma'\gamma}^\dagger] \\ &= \sum_{\alpha'\gamma'} U_{CP,\alpha\alpha'} U_{CP,\gamma'\gamma}^\dagger \langle \hat{c}_{-i\alpha'}^\dagger(t) \hat{c}_{-j\gamma'} \rangle, \end{aligned}$$

which is equivalent to

$$\langle \hat{c}_{\mathbf{k}\alpha}(t) \hat{c}_{\mathbf{k}\gamma}^\dagger \rangle = \sum_{\alpha'\gamma'} U_{CP,\alpha\alpha'} U_{CP,\gamma'\gamma}^\dagger \langle \hat{c}_{\mathbf{k}\alpha'}^\dagger \hat{c}_{\mathbf{k}\gamma'}(-t) \rangle.$$

Here, Z denotes the partition function. In a similar way, we obtain

$$\langle \hat{c}_{\mathbf{k}\gamma}^\dagger \hat{c}_{\mathbf{k}\alpha}(t) \rangle = \sum_{\alpha'\gamma'} U_{CP,\alpha\alpha'} U_{CP,\gamma'\gamma}^\dagger \langle \hat{c}_{\mathbf{k}\gamma'}(-t) \hat{c}_{\mathbf{k}\alpha'}^\dagger \rangle.$$

Namely, the above calculations yield the following relation between the retarded and the advanced Green's function:

$$\langle \hat{c}_{\mathbf{k}\alpha}(t) \hat{c}_{\mathbf{k}\gamma}^\dagger + \hat{c}_{\mathbf{k}\gamma}^\dagger \hat{c}_{\mathbf{k}\alpha}(t) \rangle \theta(t) = \sum_{\alpha'\gamma'} U_{CP,\alpha\alpha'} U_{CP,\gamma'\gamma}^\dagger \langle \hat{c}_{\mathbf{k}\gamma'}(t') \hat{c}_{\mathbf{k}\alpha'}^\dagger + \hat{c}_{\mathbf{k}\alpha'}^\dagger \hat{c}_{\mathbf{k}\gamma'}(t') \rangle \theta(-t').$$

with $t' = -t$. We note that the right (left) hand side of the above equation corresponds to iG^R ($-iG^A$), respectively.

Applying the Fourier transformation, we obtain Eq. (35).

¹⁵⁸ Eq. (36) can be obtained by making use of Hermiticity of the Hamiltonian. With the Lehmann representation, the Green's function can be written as

$$G_{\alpha\beta}(\omega + i\delta, \mathbf{k}) = Z^{-1} \sum_{nm} e^{-\beta E_n} \frac{e^{\beta(E_n - E_m)} + 1}{(\omega + i\delta + E_n - E_m)} \langle n | \hat{c}_{\mathbf{k}\alpha} | m \rangle \langle m | \hat{c}_{\mathbf{k}\beta}^\dagger | n \rangle,$$

where $|n\rangle$'s are eigenstates of the Hamiltonian \hat{H} . Z denotes the partition function $Z := \sum_n e^{-\beta E_n}$. With this representation, we can see that the following relation holds:

$$\begin{aligned} G_{\beta\alpha}^*(\omega + i\delta, \mathbf{k}) &= Z^{-1} \sum_{nm} e^{-\beta E_n} \frac{e^{\beta(E_n - E_m)} + 1}{(\omega + i\delta + E_n - E_m)^*} \langle n | \hat{c}_{\mathbf{k}\beta} | m \rangle^* \langle m | \hat{c}_{\mathbf{k}\alpha}^\dagger | n \rangle^* \\ &= Z^{-1} \sum_{nm} e^{-\beta E_n} \frac{e^{\beta(E_n - E_m)} + 1}{(\omega - i\delta + E_n - E_m)} \langle n | \hat{c}_{\mathbf{k}\alpha} | m \rangle \langle m | \hat{c}_{\mathbf{k}\beta}^\dagger | n \rangle \\ &= G_{\alpha\beta}(\omega - i\delta, \mathbf{k}), \end{aligned}$$

which is nothing but the relation shown in Eq. (36).

¹⁵⁹ Eq. (39a) can be obtained as follows. Firstly, we note that the following relations hold:

$$\begin{aligned} it\hat{H} &= it\hat{U}_\Gamma \hat{H}^* \hat{U}_\Gamma^\dagger, \\ \hat{U}_\Gamma \hat{c}_{i\alpha} \hat{U}_\Gamma^\dagger &= \sum_\beta U_{\Gamma,\alpha\beta} \hat{c}_{i\beta}^\dagger, \\ \langle n^* | \hat{A} | m^* \rangle &= \langle m | \hat{A}^T | n \rangle, \end{aligned}$$

where $|n\rangle$ and $|m\rangle$ are arbitrary states. $|n^*\rangle$ is defined as $|n^*\rangle := \sum_{\{i\alpha\}} |\{i\alpha\}\rangle \langle n|\{i\alpha\}\rangle$ with the states $|\{i\alpha\}\rangle$ obtained by applying the operators $\hat{c}_{i\alpha}^\dagger$ to the vacuum. By using the above relations, $\langle \hat{c}_{i\alpha}(t) \hat{c}_{j\gamma}^\dagger \rangle$ is rewritten as

$$\begin{aligned} \langle \hat{c}_{i\alpha}(t) \hat{c}_{j\gamma}^\dagger \rangle &= Z^{-1} \text{tr}[e^{-\beta \hat{H}} e^{it\hat{H}} \hat{c}_{i\alpha} e^{-it\hat{H}} \hat{c}_{j\gamma}^\dagger] \\ &= Z^{-1} \text{tr}[e^{-\beta \hat{H}^*} e^{it\hat{H}^*} \hat{U}_\Gamma^\dagger \hat{c}_{i\alpha} \hat{U}_\Gamma e^{-it\hat{H}^*} \hat{U}_\Gamma^\dagger \hat{c}_{j\gamma}^\dagger \hat{U}_\Gamma] \\ &= Z^{-1} \sum_{\alpha'\gamma'} \text{tr}[e^{-\beta \hat{H}^*} e^{it\hat{H}^*} U_{\Gamma,\alpha\alpha'} \hat{c}_{i\alpha'}^\dagger e^{-it\hat{H}^*} \hat{c}_{i\gamma'} U_{\Gamma,\gamma'\gamma}^\dagger] \\ &= Z^{-1} \sum_{\alpha'\gamma'} U_{\Gamma,\alpha\alpha'} U_{\Gamma,\gamma'\gamma}^\dagger \text{tr}[e^{-\beta \hat{H}} e^{it\hat{H}} \hat{c}_{i\gamma'}^\dagger e^{-it\hat{H}} \hat{c}_{i\alpha'}] \\ &= \sum_{\alpha'\gamma'} U_{\Gamma,\alpha\alpha'} U_{\Gamma,\gamma'\gamma}^\dagger \langle \hat{c}_{i\gamma'}^\dagger \hat{c}_{i\alpha'}(-t) \rangle, \end{aligned}$$

which is equivalent to

$$\langle \hat{c}_{\mathbf{k}\alpha}(t) \hat{c}_{\mathbf{k}\gamma}^\dagger \rangle = \sum_{\alpha'\gamma'} U_{\Gamma,\alpha\alpha'} U_{\Gamma,\gamma'\gamma}^\dagger \langle \hat{c}_{\mathbf{k}\gamma'}^\dagger \hat{c}_{\mathbf{k}\alpha'}(-t) \rangle.$$

Here, Z denotes the partition function. In a similar way, we obtain

$$\langle \hat{c}_{\mathbf{k}\gamma}^\dagger \hat{c}_{\mathbf{k}\alpha}(t) \rangle = \sum_{\alpha'\gamma'} U_{\Gamma,\alpha\alpha'} U_{\Gamma,\gamma'\gamma}^\dagger \langle \hat{c}_{\mathbf{k}\alpha'}(-t) \hat{c}_{\mathbf{k}\gamma'}^\dagger \rangle.$$

Namely, the above calculation yields the following relation between the retarded and the advanced Green's function:

$$\langle \hat{c}_{\mathbf{k}\alpha}(t) \hat{c}_{\mathbf{k}\gamma}^\dagger + \hat{c}_{\mathbf{k}\gamma}^\dagger \hat{c}_{\mathbf{k}\alpha}(t) \rangle \theta(t) = \sum_{\alpha'\gamma'} U_{\Gamma,\alpha\alpha'} U_{\Gamma,\gamma'\gamma}^\dagger \langle \hat{c}_{\mathbf{k}\alpha'}(t') \hat{c}_{\mathbf{k}\gamma'}^\dagger + \hat{c}_{\mathbf{k}\gamma'}^\dagger \hat{c}_{\mathbf{k}\alpha'}(t') \rangle \theta(-t'),$$

with $t' = -t$. We note that the right (left) hand side of the above equation corresponds to iG^R ($-iG^A$), respectively. With the Fourier transformation and Eq. (36) we obtain Eq. (39a).

- ¹⁶⁰ T. Yoshida and Y. Hatsugai, Phys. Rev. B **100**, 054109 (2019).
¹⁶¹ C.-H. Liu, H. Jiang, and S. Chen, Phys. Rev. B **99**, 125103 (2019).
¹⁶² J. C. Y. Teo and C. L. Kane, Phys. Rev. B **82**, 115120 (2010).
¹⁶³ C.-K. Chiu and A. P. Schnyder, Phys. Rev. B **90**, 205136 (2014).
¹⁶⁴ T. Morimoto and A. Furusaki, Phys. Rev. B **88**, 125129 (2013).
¹⁶⁵ K. Shiozaki and M. Sato, Phys. Rev. B **90**, 165114 (2014).
¹⁶⁶ T. c. v. Bzdusek and M. Sigrist, Phys. Rev. B **96**, 155105 (2017).
¹⁶⁷ T. Takimoto, Journal of the Physical Society of Japan **80**, 123710 (2011).
¹⁶⁸ M. Neupane, N. Alidoust, S.-Y. Xu, T. Kondo, Y. Ishida, D. J. Kim, C. Liu, I. Belopolski, Y. J. Jo, T.-R. Chang, H.-T. Jeng, T. Durakiewicz, L. Balicas, H. Lin, A. Bansil, S. Shin, Z. Fisk, and M. Z. Hasan, Nature Communications **4**, 2991 (2013).
¹⁶⁹ J. Jiang, S. Li, T. Zhang, Z. Sun, F. Chen, Z. R. Ye, M. Xu, Q. Q. Ge, S. Y. Tan, X. H. Niu, M. Xia, B. P. Xie, Y. F. Li, X. H. Chen, H. H. Wen, and D. L. Feng, Nature Communications **4**, 3010 (2013).
¹⁷⁰ N. Xu, X. Shi, P. K. Biswas, C. E. Matt, R. S. Dhaka, Y. Huang, N. C. Plumb, M. Radović, J. H. Dil, E. Pomjakushina, K. Conder, A. Amato, Z. Salman, D. M. Paul, J. Mesot, H. Ding, and M. Shi, Phys. Rev. B **88**, 121102 (2013).
¹⁷¹ R. Peters, T. Yoshida, H. Sakakibara, and N. Kawakami, Phys. Rev. B **93**, 235159 (2016).
¹⁷² R. Peters, T. Yoshida, and N. Kawakami, Phys. Rev. B **98**, 075104 (2018).
¹⁷³ P. Thunström and K. Held, arXiv preprint arXiv:1907.03899 (2019).
¹⁷⁴ H. Weng, J. Zhao, Z. Wang, Z. Fang, and X. Dai, Phys. Rev. Lett. **112**, 016403 (2014).
¹⁷⁵ K. Hagiwara, Y. Ohtsubo, M. Matsunami, S.-i. Ideta, K. Tanaka, H. Miyazaki, J. E. Rault, P. L. Fteivre, F. Bertran, A. Taleb-Ibrahimi, R. Yukawa, M. Kobayashi, K. Horiba, H. Kumigashira, K. Sumida, T. Okuda, F. Iga, and S.-i. Kimura, Nature Communications **7**, 12690 (2016).
¹⁷⁶ T. Helbig, T. Hofmann, S. Imhof, M. Abdelghany, T. Kiessling, L. W. Molenkamp, C. H. Lee, A. Szameit, M. Greiter, and R. Thomale, arXiv preprint arXiv:1907.11562 (2019).
¹⁷⁷ T. Hofmann, T. Helbig, F. Schindler, N. Salgo, M. Brzezińska, M. Greiter, T. Kiessling, D. Wolf, A. Vollhardt, A. Kabaši, *et al.*, arXiv preprint arXiv:1908.02759 (2019).
¹⁷⁸ T. Yoshida, T. Mizoguchi, and Y. Hatsugai, arXiv preprint arXiv:1912.12022 (2019).
¹⁷⁹ H. Jiang, L.-J. Lang, C. Yang, S.-L. Zhu, and S. Chen, Phys. Rev. B **100**, 054301 (2019).
¹⁸⁰ N. Matsumoto, K. Kawabata, Y. Ashida, S. Furukawa, and M. Ueda, arXiv preprint arXiv:1912.09045 (2019).
¹⁸¹ C.-X. Guo, X.-R. Wang, and S.-P. Kou, arXiv preprint arXiv:2001.04209 (2020).